

A spatially resolved radio spectral study of the galaxy M51

L. Gajović¹, B. Adebahr^{2,3}, A. Basu^{4,5}, V. Heesen¹, M. Brüggem¹, F. de Gasperin⁶, M. A. Lara-Lopez⁷, J. B. R. Oonk^{8,3}, H. W. Edler¹, D. J. Bomans², R. Paladino⁶, L. E. Garduño⁹, O. López-Cruz⁹, M. Stein², J. Fritz¹⁰, J. Piotrowska¹¹, and A. Sinha⁴

¹ Hamburger Sternwarte, University of Hamburg, Gojenbergsweg 112, 21029 Hamburg, Germany

² Ruhr University Bochum, Faculty of Physics and Astronomy, Astronomical Institute (AIRUB), Universitätsstrasse 150, 44801 Bochum, Germany

³ ASTRON, PO Box 2, 7990 AA Dwingeloo, The Netherlands

⁴ Thüringer Landessternwarte, Sternwarte 5, 07778 Tautenburg, Germany

⁵ Max-Planck-Institut für Radioastronomie, Auf dem Hügel 69, 53121 Bonn, Germany

⁶ INAF - Istituto di Radioastronomia, via P. Gobetti 101, 40129 Bologna, Italy

⁷ Departamento de Física de la Tierra y Astrofísica, Instituto de Física de Partículas y del Cosmos, IPARCOS. Universidad Complutense de Madrid (UCM), E-28040, Madrid, Spain

⁸ Leiden Observatory, Leiden University, PO Box 9513, NL-2300 RA Leiden, The Netherlands

⁹ Instituto Nacional de Astrofísica, Óptica y Electrónica (INAOE), Coor. de Astrofísica, Luis Enrique Erro No.1, Tonantzintla, Puebla, México C.P. 72840.

¹⁰ Instituto de Radioastronomía y Astrofísica, UNAM, Campus Morelia, A.P. 3-72, C.P. 58089, Mexico

¹¹ Astronomical Observatory of the Jagiellonian University, ul. Orła 171, 30-244 Kraków, Poland

Received - / Accepted -

ABSTRACT

Context. Radio continuum emission from galaxies at gigahertz frequencies can be used as an extinction-free tracer of star formation. However, at frequencies of a few hundred megahertz, there is evidence for low-frequency spectral flattening.

Aims. We wish to better understand the origin of this low-frequency flattening and, to this end, perform a spatially resolved study of the nearby spiral galaxy M51. We explore the different effects that can cause flattening of the spectrum towards lower frequencies, such as free-free absorption and cosmic-ray ionisation losses.

Methods. We used radio continuum intensity maps between 54 and 8350 MHz at eight different frequencies, with observations at 240 MHz from the Giant Metrewave Radio Telescope presented for the first time. We corrected for contribution from thermal free-free emission using an H α map that has been extinction-corrected with 24 μ m data. We fitted free-free absorption models to the radio spectra to determine the emission measure (EM) as well as polynomial functions to measure the non-thermal spectral curvature. We also obtained a new extinction-corrected H α intensity map from the Metal-THINGS survey using integral field unit spectroscopy.

Results. The non-thermal low-frequency radio continuum spectrum between 54 and 144 MHz is very flat and even partially inverted, particularly in the spiral arms; contrary, the spectrum at higher frequencies shows the typical non-thermal radio continuum spectrum. However, we do not find any correlation between the EMs calculated from radio and from H α observations; instead, the non-thermal spectral curvature weakly correlates with the H I gas mass surface density. This suggests that cosmic-ray ionisation losses play an important role in the low-frequency spectral flattening.

Conclusions. The observed spectral flattening towards low frequencies in M51 is caused by a combination of ionisation losses and free-free absorption. The reasons for this flattening need to be understood in order to use sub-GHz frequencies as a star-formation tracer.

Key words. galaxies: ISM - galaxies: individual: M51 - galaxies: spiral - galaxies: star formation - radiation mechanisms: general - radio continuum: ISM

1. Introduction

At radio frequencies of a few gigahertz and below, the majority of continuum emission from galaxies is non-thermal synchrotron radiation produced by cosmic-ray electrons (Niklas et al. 1997; Basu et al. 2012; Tabatabaei et al. 2017). These cosmic rays are accelerated in the shock-front of supernovae explosions, and therefore they originate from regions with higher star formation (Green 2014). The integrated spectrum of nearby galaxies at gigahertz frequencies (approximately 0.5–10 GHz) mostly follows a power law where the flux density scales with frequency as $S_\nu \propto \nu^\alpha$; the radio spectral index α has values between -1.2 and -0.5 (Gioia et al. 1982; Li et al. 2016; Tabatabaei et al. 2017). If frequencies below approximately 300 MHz are included though,

the observed spectra are curved with the spectral curvature of $\beta = -0.2$, which denotes the change in spectral index per logarithmic frequency decade assuming constant curvature (Marvil et al. 2015).

While the value for the radio spectral index generally agrees with models of the overall injection spectrum of cosmic rays from supernovae ($\alpha \approx -0.5$; Blandford & Eichler 1987), including their energy losses mainly due to synchrotron and inverse Compton radiation while propagating away from their origin (Gioia et al. 1982; Beck & Wielebinski 2013; Han 2017), the origin of the curvature is still a matter of debate (Basu et al. 2015; Mulcahy et al. 2018). Pohl & Schlickeiser (1990) and Pohl et al. (1991a,b) provide an explanation for curved spectra via a combination of ionisation and electronic excitation (Gould 1975),

inverse Compton radiation, synchrotron radiation, and relativistic bremsstrahlung, which would cause a smooth change in the spectral index of $\Delta\alpha = 0.5$ from higher to lower radio frequencies. On the other hand, [Israel & Mahoney \(1990\)](#) observed a dependence of the curvature with the inclination of the galaxies and concluded that a fragmented cool ionised medium with temperatures of 500–1000 K is responsible for the curvature by thermally absorbing a part of the emitted synchrotron emission at lower frequencies. However, [Hummel \(1991\)](#) used the same data as [Israel & Mahoney \(1990\)](#) and could not find any correlation between the curvature in the sampled galaxies and their inclinations. A more recent study by [Chyży et al. \(2018\)](#) using additional data from the LOFAR Multifrequency Snapshot Sky Survey (MSSS) at 150 MHz ([Heald et al. 2015](#)) confirmed the results by [Hummel \(1991\)](#).

Furthermore, integrated spectra of star-forming galaxies encompass a mixture of the complex interplay between thermal and non-thermal components and different energy loss and propagation effects in the most likely non-isotropic and inhomogeneous medium ([Basu et al. 2015](#); [Lisenfeld & Völk 2000](#)). Studies of large samples of these objects are therefore limited by obtaining high-quality, high-resolution observations at low radio frequencies ($\lesssim 300$ MHz). Advancements in data calibration and imaging techniques at these low-frequencies, especially for radio interferometers such as the LOw Frequency ARray (LOFAR; [Tasse 2014](#); [Tasse et al. 2018](#)) and the Giant Metrewave Telescope (GMRT; [Intema et al. 2009](#); [Intema 2014](#); [Intema et al. 2017](#)), now allow the production of high dynamic range images with resolutions matching those of observations performed at gigahertz frequencies.

Spatially resolved studies are currently limited to nearby objects where individual star-forming regions can be analysed, and the radio emission of spiral arm, inter-arm and surrounding regions can be separated. [Roy & Pramesh Rao \(2006\)](#) showed that thermal absorption plays a key role in shaping the spectra of the centre of the Milky Way below 500 MHz while its integrated-spectrum turns over at about 3 MHz ([Brown 1973](#)). Turnovers have also been detected for individual sources in the starburst galaxy M 82 ([Adebahr et al. 2017](#)) and the integrated flux densities for the core regions of M 82 ([Adebahr et al. 2013](#)) and Arp 220 ([Varenius et al. 2016](#)) at around 1000 MHz. For these two objects a flattening was also observed for the integrated (global) radio spectra ([Klein et al. 1988](#); [Condon 1992](#); [Anantharamaiah et al. 2000](#)), just like in the starburst galaxy NGC 253 ([Marvil et al. 2015](#)). Several of the compact H II regions in the dwarf galaxy IC 10 show evidence of thermal free-free absorption in the radio spectra of the 320 MHz observations ([Basu et al. 2017](#)). Recently, evidence of low frequency absorption was also found in region of the edge-on galaxy NGC 4631 with a very flat radio spectrum ([Stein et al. 2023](#)). Local spectral turnovers were also observed in jellyfish galaxies, possibly due to gas compression and subsequent ionization losses ([Lal et al. 2022](#); [Ignesti et al. 2022](#); [Roberts et al. 2023](#)).

We choose M 51 as the target primarily as it benefits from multi-frequency radio continuum data. Also, the face-on orientation and the proximity are important because they make it easier to resolve and separate the spiral arms. Other properties of M 51 are listed in Table 1. The entire galaxy is now mapped at 54 and 144 MHz with LOFAR ([de Gasperin et al. 2021](#); [Shimwell et al. 2022](#)). Furthermore, there are data at 1370 and 1699 MHz taken with the Westerbork Synthesis Radio Telescope (WSRT; [Braun et al. 2007](#)). At even higher frequencies, [Fletcher et al. \(2011\)](#) presented maps taken with the Very Large Array (VLA) at 4850 and 8350 MHz. VLA maps were combined with maps observed

Table 1: Basic properties of M51.

Name	M 51
Alternative names	NGC 5194/5155
RA ₂₀₀₀	13 ^h 29 ^m 56 ^s .2
DEC ₂₀₀₀	+47° 13' 50"
Type	Galaxy Pair (Sa + Sc) ^a
Apparent size (D ₂₅)	9'
Distance	8.58 ± 0.10 Mpc ^b
Position angle	12°0'
Inclination angle	-20.3° ^c

References: ^a[Karachentsev et al. \(1985\)](#), ^b[McQuinn et al. \(2016\)](#), ^c[Hu et al. \(2013\)](#)

with the 100-m Effelsberg telescope in order to observe all angular scales. These data were analysed by [Heesen et al. \(2023\)](#) who studied the transport of cosmic-ray electrons at kpc-scales and found it to be energy-independent diffusion for electrons with energies below 10 GeV.

In this paper we extend the data with a new 240 MHz map from the Giant Metre Radio Telescope. We used eight data-sets observed at five different radio facilities (LOFAR, GMRT, WSRT, VLA, Effelsberg) over the frequency range 54–8350 MHz to perform a spatially resolved radio spectral study of the nearby spiral galaxy M 51. For the first time we were able to separate the actively star-forming and non star-forming regions of a nearby galaxy down to frequencies as low as 54 MHz. This allows us to investigate the relation between star-formation and the flattening of the radio spectrum, as well as to perform an examination of the origin of the flattening.

This article is structured as follows. In Sect. 2 we present our dataset spanning nine frequency windows. Section 3 describes how we conduct the main data analysis which includes subtraction of thermal emission (Sect. 3.2), spectral index maps (Sect. 3.4), separation of galaxy regions (Sect. 3.3), and comparison of low- and high-frequency spectral indices (Sect. 3.5). Spectral index flattening and low-frequency turnovers are investigated in Sect. 4. We summarize and conclude in Sect. 5.

2. Data handling

2.1. Giant Metrewave Radio Telescope observations

We have analyzed archival, so far not published, data of M 51 at 240 MHz, observed with the Giant Metrewave Radio Telescope (GMRT; [Swarup et al. 1991](#)) using the old hardware correlator (project code: 10AFA01). The map is presented here for the first time, see Fig. 1. The data were recorded by splitting the 16 MHz bandwidth into two bands of 8 MHz each covered using 64 125-kHz wide channels, the upper and lower sidebands, USB and LSB, respectively. We have analyzed only the USB data centered at 241.25 MHz because the LSB data were unusable due to radio frequency interference (RFI) and correlator-related errors. The total duration of these observations is 11 h, wherein 4 min scans on a nearby, bright, point source, 3C 286, were interleaved every 25 min. 3C 286 was used to calibrate the flux scale, bandpass and phase. Additional 15 min scans on 3C 286 were performed at the beginning and end of the observations run. In these observations, a total of 8.3 h was spent on M 51. The data were analyzed in AIPS¹ using the standard analysis protocol

¹ AIPS, the Astronomical Image Processing System, is free software available from the National Radio Astronomy Observatory.

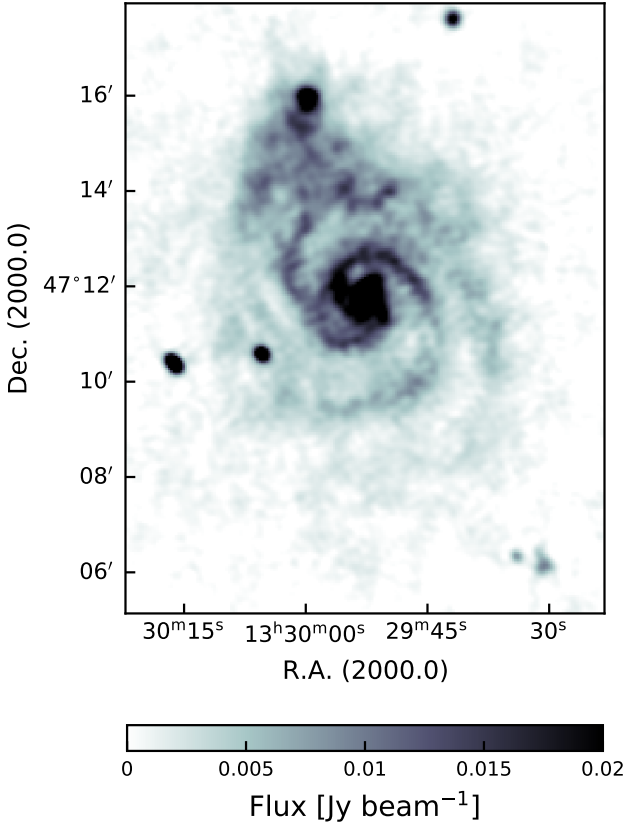


Fig. 1: Radio continuum map of M 51 at 240 MHz observed with the GMRT. The map has an angular resolution of $14'0'' \times 12'2''$ and an rms noise of $500 \mu\text{Jy beam}^{-1}$.

at low frequencies. Data were manually inspected, and data affected by RFI and bad baselines were flagged using the TVFLG, WIPER and SPFLG tasks. The task FLGIT was used to automatically remove RFI-affected frequency channels that have residual spectral flux above 4σ level. Overall, in these observations, less than $\sim 35\%$ of the data were found to be corrupted in the USB, including three non-working antennas and corrupted baselines. We used the Baars et al. (1977) absolute flux density scale to determine the flux density of $29.5 \pm 1.6 \text{ Jy}$ at 241.25 MHz for 3C 286.² RFI-removal and determining gain solutions were iteratively performed, and when the closure-phase errors determined using 3C 286 were below 1%, solutions were applied to the target M 51.

The task IMAGR was used to deconvolve the calibrated data. In order to minimize the effect of wide-field imaging with non-coplanar baselines, we used polyhedron imaging (Cornwell & Perley 1992) by subdividing the field of view ($\approx 3.7^\circ$) into $9 \times 9 = 81$ smaller facets. After flagging the first and the last two channels, we vector-averaged four adjacent frequency channels of 125 kHz each into 15 500-kHz-channels to ensure that the bandwidth smearing near 240 MHz is less than the size of the synthesized beam. Thus, the final image was made using 7.5 MHz bandwidth. Five rounds of phase-only self-calibration were performed by choosing point sources above 8σ using the task CCSEL. The solution interval was progressively reduced dur-

² Note that, the flux density of 3C 286 obtained with the Baars et al. (1977) is consistent with 28.15 Jy from the Perley & Butler (2017a) absolute scale within the error.

ing each round, starting from 3 min at the start to 0.5 min in the last round. Additional flagging were also done after each round until in the fifth round, the closure-phase error was below 0.5%. To prepare the final image, we employed the SDI clean algorithm (Steer et al. 1984) to deconvolve the extended emission in M 51. After ensuring that point-like emission were cleaned using BGC clean algorithm, SDI clean was used, and the clean-box masks were manually changed in order to deconvolve different scales. The final image at 240 MHz used in this work was produced at an angular resolution of $14'0'' \times 12'2''$ with an rms noise of $\approx 500 \mu\text{Jy beam}^{-1}$. While not a very sensitive map, it suffices for our analysis. The galaxy-integrated flux density of M 51 at 240 MHz within the 3σ contour is found to be $6.07 \pm 0.63 \text{ Jy}$. As can be seen in Fig. 3, the total flux density of M 51 agrees well with those in the literature when interpolated from higher and lower frequency observations.

The uncertainties in the estimated flux density depend on the absolute flux scale error and on the errors associated with uncalibrated system temperature (T_{sys}) variations (Basu et al. 2012). The absolute flux scale error for 3C 286 is found to be 5.4% (Baars et al. 1977), and the T_{sys} variation for the old GMRT system, as used for the observations in this paper, was estimated to be $\sim 5\%$ (Roy & Rao 2004). So, the overall systematic error, added in quadrature, is expected to be $\sim 7.5\%$. We use a slightly more conservative value of 10% for the systematic flux error of the GMRT data. The statistical measurement error due to the rms noise in the map is added on top of that, but that contribution is relatively small.

2.2. Archival radio continuum observations

In total, radio continuum image data of M 51 were collected in nine different frequency bands between 54 MHz and 8350 MHz (see Table 2). All retrieved images were inspected for artefacts and their integrated fluxes cross-checked with literature values. Preferentially single-dish or compact interferometric measurements were used to ensure that our images are not affected by the missing spacing problem.

The lowest frequency image at 54 MHz is from the LOFAR LBA Sky Survey (LoLSS; de Gasperin et al. 2021) using the low-band antennae. Flux calibrators were used to calibrate direction-independent effects as well as the bandpass response of the instrument. Additionally, the flux density of sources in the survey was compared to the Rees survey (8C; Hales et al. 1995) at 38 MHz, the Very Large Array (VLA) Low-Frequency Sky Survey redux (VLSSr; Lane et al. 2012) at 74 MHz, the LOFAR Two-metre Sky Survey data release 2 (LoTSS-DR2; Shimwell et al. 2022) at 144 MHz, and the NRAO VLA Sky Survey (NVSS; Condon et al. 1998) at 1400 MHz. A conclusive estimate of the flux density accuracy could not be derived, but it is suggested that assuming a conservative 10% error on the LoLSS flux density scale is beneficial (de Gasperin et al. 2021). Heesen et al. (2022) investigated 45 nearby galaxies in LoTSS-DR2 including M 51, we use their re-processed map of M 51. They confirmed that the integrated flux densities of the $6''$ and $20''$ maps are identical for the same integration area. This ensures that the high-resolution map, which we are using, is sufficiently deconvolved. The flux densities in the work by Heesen et al. (2022) were matched with the LoTSS-DR2 scale which is has an error below 10% (Shimwell et al. 2022). Therefore, in this work we assume a flux uncertainty of 10% for the LoTSS map.

The GMRT map at 333 MHz was already presented by Mulcahy et al. (2016). They have used it for an analysis of the large-scale diffuse emission of M 51 and found no issues in re-

Table 2: Observation parameters for the nine radio maps used in the analysis.

Telescope (Survey)	Central frequency [MHz]	Beam size	σ rms noise [μ Jy]	convolved σ_c rms noise [μ Jy]	Flux uncertainty ϵ_v [%]	Reference
LOFAR (LoLSS)	54	15'0 × 15'0	1500	1500	10	1
LOFAR (LoTSS)	144	6'0 × 6'0	45	100	10	2
GMRT	240	14'0 × 12'2	500	850	10	3
GMRT	333	15'0 × 15'0	200	350	10	4
GMRT ^a	619	5'7 × 4'6	27	125	10	5
WSRT (SINGS)	1370	17'5 × 12'5	22	25	5	6
WSRT (SINGS)	1699	13'5 × 10'0	27	30	5	6
VLA + Effelsberg	4850	15'0 × 15'0	30	30	5	7
VLA + Effelsberg	8350	15'0 × 15'0	20	20	5	7

References: 1) [de Gasperin et al. \(2021\)](#), 2) [Shimwell et al. \(2022\)](#), 3) This work, 4) [Mulcahy et al. \(2016\)](#), 5) [Farnes et al. \(2013\)](#), 6) [Braun et al. \(2007\)](#), 7) [Fletcher et al. \(2011\)](#)

^a Map not used in the analysis due to possible deconvolution errors.

lation to missing emission for the inner part of the disc. In contrast, the 619 MHz GMRT image of [Farnes et al. \(2013\)](#) showed a ‘negative bowl’ around the diffuse emission of M 51 indicating deconvolution errors arising from missing emission. We have, therefore, refrained from using the diffuse emission for further quantitative analyses. However, we believe that the bright emissions on small-scales, especially in the inner parts of the galaxy to be less affected from missing flux issues. The WSRT images at 1370 and 1699 MHz from [Braun et al. \(2007\)](#) were cross-checked with the VLA image at 1400 MHz published in [Fletcher et al. \(2011\)](#) and with literature flux density values. No differences in flux densities or morphology were found. The WSRT-SINGS observations were bracketed by observations of the total intensity calibration sources yielding an absolute flux density calibration accuracy better than 5% [Braun et al. \(2007\)](#). We therefore assume 5% flux uncertainty for the WSRT maps used in this work. Finally, the VLA images at 4850 and 8350 MHz have already been combined with single-dish Effelsberg telescope data as described in [Fletcher et al. \(2011\)](#), so that we do not expect any missing flux. Flux measurement errors are usually assumed to be 5% for VLA data [Konar et al. \(2013\)](#).

We convolved all images to the largest common beam of 17'5 × 15'0 (see Table 2) using the routine CONVOL of the Multichannel Image Reconstruction, Image Analysis and Display (MIRIAD, [Sault et al. 1995](#)) software package. All images were then aligned to a common world coordinate system, re-gridded to a pixel size of 3'', and transformed to the reference pixel and image size. This was achieved using the REGRID routine of MIRIAD. The rms noise, σ , of each individual image was determined by calculating the standard deviation over an emission-free area. For further analysis, only pixels above 4.5 σ were considered.

We assumed an absolute flux scale uncertainty of 10% for the low frequency data (for LOFAR and GMRT) and 5% for all other data (see Table 2). These estimates incorporate all errors and are conservative. There are several contributions, first there is the accuracy of the absolute flux density of the calibrator models. This is 3–5% ([Perley & Butler 2017b](#)). However, for spectral index studies like our work the relative scale is more

relevant, the uncertainty of which is around 1%. Deconvolution errors are around 1% but increase at low signal-to-noise ratios ([Offringa et al. 2014](#)). The background noise can be neglected except for local measurements, where we add the rms noise in quadrature. Other errors such as the uncertainty of primary beam correction can be also neglected as the primary beam size is much larger than the size of source. For the combined VLA and Effelsberg maps the uncertainty is limited by the feathering procedure which allows one to combine the interferometric and single-dish images ([Cotton 2017](#)). Their uncertainty may be higher in areas of low signal-to-noise ratios, but we restrict most of our analysis to areas where this should make no strong difference.

2.3. Integral field unit spectroscopy

We complement our radio continuum data with new optical integral field unit spectroscopy data from the Metal-THINGS survey ([Lara-López et al. 2021](#)). Metal-THINGS is a survey of nearby galaxies observing with the George Mitchell and Cynthia Spectrograph (GCMS; formerly known as VIRUS-P), mounted to the 2.7-m Harlan J. Smith telescope located at the McDonald Observatory in Texas. The integral field unit (IFU) has a field of view of 100'' × 102''. Due to the large angular size of M 51, a total of 12 pointings were needed to cover the entire galaxy. The spectroscopic data were processed with the spectral synthesis code STARLIGHT ([Cid Fernandes et al. 2011](#)) as described in [Lara-López et al. \(2021, 2023\)](#). We used an H α flux map corrected for extinction, where the correction was performed using the Balmer decrement. The map is shown in figure 2.

3. Data analysis

3.1. Integrated spectrum

We start our analysis by calculating the integrated spectrum, which can help us to assess the robustness of the data. The spectrum is plotted and compared to the integrated spectrum from [Mulcahy et al. \(2014\)](#) in Fig. 3. The integrated spectrum fol-

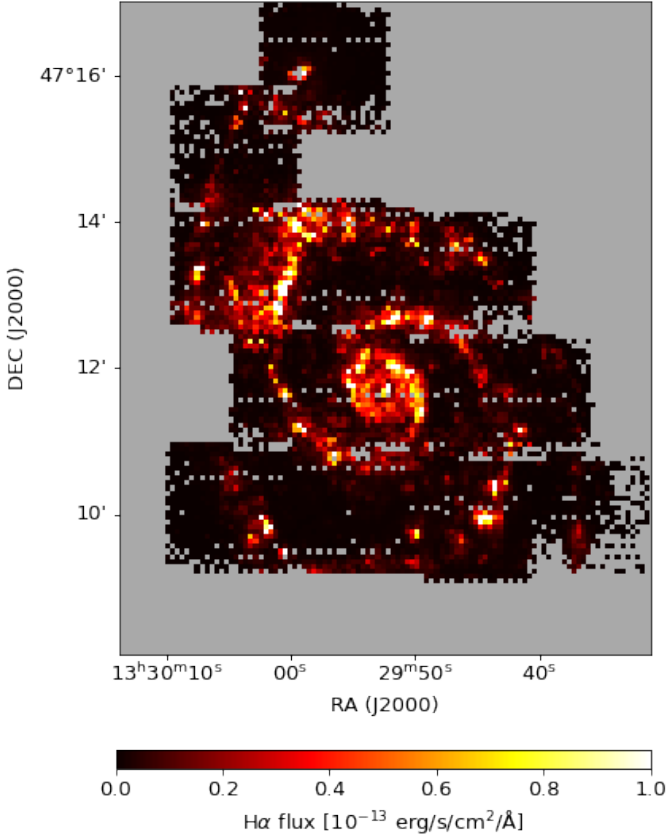


Fig. 2: H α flux density map of M51 from the Metal-THINGS survey corrected for extinction using the Balmer decrement. The gray pixels were not observed.

lows a power law with a spectral index of $\alpha = -0.80 \pm 0.05$ without any flattening at low frequencies. This is consistent with the spectral index of -0.79 ± 0.02 calculated by [Mulcahy et al. \(2014\)](#). This test confirms that the integrated flux density of M51 in our maps matches previous observations.

3.2. Separation of thermal and synchrotron emission

In order to get a better handle on the contribution of the thermal emission and separate the thermal from the non-thermal emission we used H α to estimate the free-free emission in M51. For this, we used a continuum-subtracted H α map obtained with the Kitt Peak National Observatory 2.1-m telescope using the narrow-band H α -filter KP1563 ([Kennicutt et al. 2003](#)). The map was downloaded from the ancillary data at the SINGS webpage.³ The H α image, shown in Fig. A.1, has an angular resolution of $1''.35 \times 1''.35$ and an rms noise of $\approx 50 \mu\text{Jy beam}^{-1}$. Because the H α emission is easily absorbed by the dust, the observed H α intensity $I_{\text{H}\alpha, \text{obs}}$ needs to be corrected for foreground and internal extinction.

The foreground extinction is low in the direction of M51 ([Schlafly & Finkbeiner 2011](#)); for that reason we neglected it. The internal extinction within M51 was corrected with a $24 \mu\text{m}$ mid-infrared map to obtain an extinction-corrected H α emission line flux ([Kennicutt et al. 2009](#)):

$$F_{\text{H}\alpha} = F_{\text{H}\alpha, \text{obs}} + 0.02 \nu_{24\mu\text{m}} I_{24\mu\text{m}}. \quad (1)$$

³ <http://irsa.ipac.caltech.edu/data/SPITZER/SINGS/>

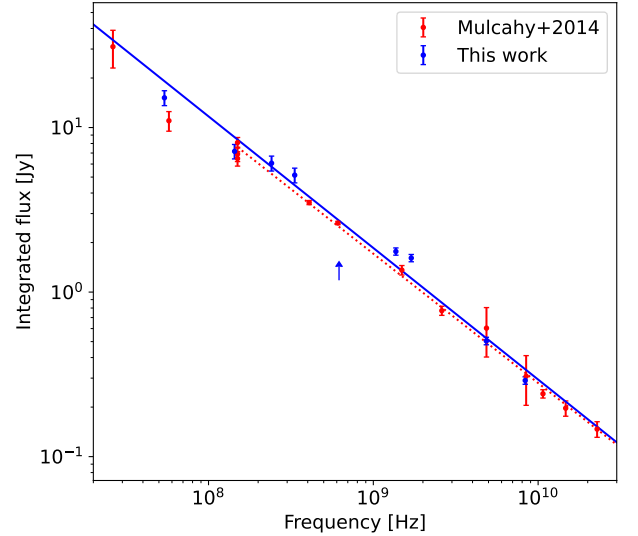


Fig. 3: Global radio continuum spectrum of M51. We show integrated flux densities calculated from our data and compare them with literature data compiled by [Mulcahy et al. \(2014\)](#). Power-law fits correspond to radio spectral indices of -0.80 ± 0.05 for our data (blue data points and solid line) and -0.79 ± 0.02 for the literature data (red data points and dotted line). The flux density at 619 MHz is only given as a lower limit and not included in the fit.

Here, $I_{24\mu\text{m}}$ is the intensity at $24 \mu\text{m}$ and is obtained from a *Spitzer* map observed as a part of the SIRTf Nearby Galaxies Survey (SINGS; [Kennicutt et al. 2003](#)). The $24 \mu\text{m}$ map has an angular resolution of $6''$. We convolved the observed H α map to $6''$ and aligned it to the the same coordinate system as that of the $24 \mu\text{m}$ map.

The thermal contribution to the radio continuum emission at a given frequency ν can then be calculated using ([Deeg et al. 1997](#))

$$\frac{S_{\text{th}}(\nu)}{\text{erg cm}^{-2} \text{ s}^{-1} \text{ Hz}^{-1}} = 1.14 \times 10^{-14} \left(\frac{\nu}{1000 \text{ MHz}} \right)^{-0.1} \times \left(\frac{T_e}{10^4 \text{ K}} \right)^{0.34} \left(\frac{F_{\text{H}\alpha}}{\text{erg cm}^{-2} \text{ s}^{-1}} \right), \quad (2)$$

where T_e is the thermal electron temperature.

The electron temperature of the ionised gas phase is usually anti-correlated with the metallicity of the corresponding H II regions ([Alloin et al. 1979](#); [Pagel et al. 1979](#); [Stasińska et al. 1981](#)). Since the metallicity usually increases towards the centre of galaxies, T_e decreases. In order to address the radial variation of T_e , we used the catalogue of H II regions in M51 from [Bresolin et al. \(2004\)](#) and followed the linear fitting procedure of [Tremblin et al. \(2014\)](#) to calculate its radial profile. The data with the fit are shown in Fig. 4. The electron temperature T_e is found to follow the relation

$$\frac{T_e}{\text{K}} = (266 \pm 47) \left(\frac{R_{\text{gal}}}{\text{kpc}} \right) + (4533 \pm 374), \quad (3)$$

where R_{gal} is the galactocentric distance. We note here that the T_e measured in [Bresolin et al. \(2004\)](#) are derived from auroral lines, which are only detectable in low-metallicity H II regions.

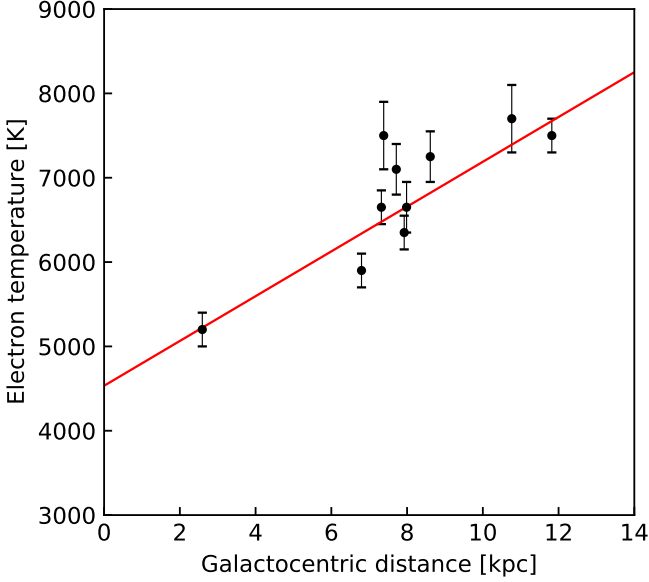


Fig. 4: Electron temperature T_e measured in H II regions as function of galactocentric distance R_{gal} . Data taken from Bresolin et al. (2004). The red line represents the best linear fit.

This could cause a bias towards higher temperatures in our profile, since temperature and gas metallicity anti-correlate, and so for higher metallicities one is not anymore able to detect auroral lines. However, the overall radial dependence should still represent the average electron temperature in the H α gas.

The extinction-corrected H α map was then convolved to our common beam of $17''.5 \times 15''.0$, and re-gridded to the same coordinate system as the radio maps. For each pixel of a radio continuum map at a given frequency ν , the thermal flux density was calculated using Eq. (2) and T_e from Eq. (3). The calculated thermal flux densities (Fig. A.1) were subtracted from the total flux densities in our radio maps. The resulting non-thermal maps were used for the majority of the following analysis.

We found thermal contributions between 0.98% and 4.8% at 54 MHz, and between 12% and 14% at 8350 MHz. Note that, for a relative error of ϵ_{th} in the estimated thermal fraction f_{th} , the relative error in the synchrotron emission fraction ($\sigma_{f_{\text{nth}}}$; where $f_{\text{nth}} = 1 - f_{\text{th}}$) is given by $\sigma_{f_{\text{nth}}} = [1 - (1 \pm \epsilon_{\text{th}}) f_{\text{th}}] / [1 - f_{\text{th}}]$ (Basu et al. 2017).⁴ That means an error of up to 20% ($\epsilon_{\text{th}} = 0.2$) in a region with $f_{\text{th}} = 0.15$ (0.05) will propagate to an error of about 5 (2) % in the estimated synchrotron emission. Adding this (in quadrature) to the flux uncertainty will increase it from 5(10) % to 6.6(10.2) % assuming an exaggerated error of 20% on the thermal fraction. Because of this, the error on the thermal fraction will not significantly affect results presented in the rest of this paper.

3.3. Spiral arm, inter-arm, and galaxy core regions

Previous work (Fletcher et al. 2011) has shown the radio continuum spectrum to be different depending on the location in the galaxy. In spiral arms the radio spectral index indicates a flat non-thermal spectrum, whereas the inter-arm regions have steeper spectra. Also, the radio continuum emission depends on

⁴ Relative error of the thermal fraction f_{th} is defined as $\epsilon_{\text{th}} = \sigma_{f_{\text{th}}} / f_{\text{th}}$, where $\sigma_{f_{\text{th}}}$ is the absolute error of f_{th} .

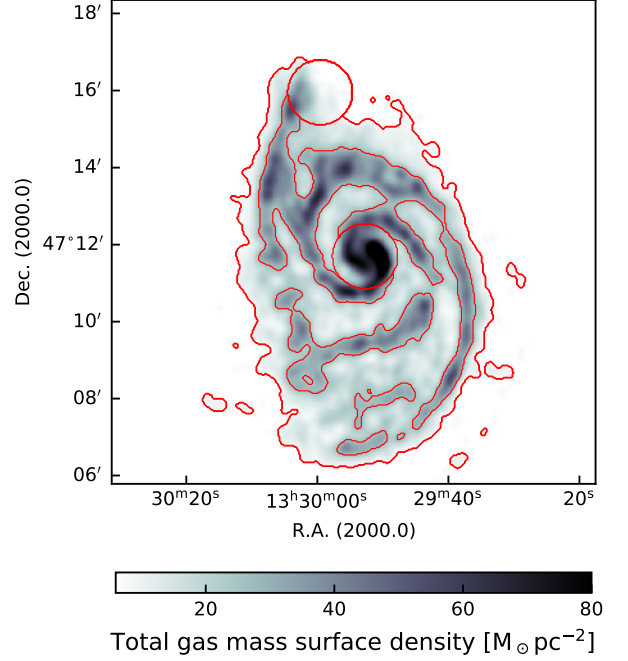


Fig. 5: Total gas mass surface density as derived from a combination of atomic (H I) and molecular (H₂) gas maps. Contours at 8 and 25 $M_{\odot} \text{pc}^{-2}$ define the borders of the spiral arm and inter-arm regions, respectively. Circular apertures denote the core regions in, both, M 51 and NGC 5195.

the star-formation rate (SFR), and this radio–SFR relation is different in the arm and inter-arm regions. Hence, we now define arm- and inter-arm regions using the distribution of the atomic and molecular gas.

We decided to follow the approach of Hitschfeld et al. (2009) using a combination of H I- and CO-maps to generate a gas surface density map, which then represents the spiral arm structure tracing the density waves (Colombo et al. 2014). To this end, we used the integrated H I map (moment 0) from Walter et al. (2008) and the integrated ¹²CO 2-1 map from Schuster et al. (2007). Both maps were convolved to our common resolution of $17''.5 \times 15''.0$. We calculate the H I column density N_{HI} using (Meyer et al. 2017):

$$N_{\text{HI}} = 1.10 \times 10^{24} \text{ cm}^{-2} \left(\frac{S_{\text{HI}}}{\text{Jy km s}^{-1}} \right) \left(\frac{a \times b}{\text{arcsec}^2} \right)^{-1}, \quad (4)$$

where S_{HI} is the velocity integrated H I flux density, and a and b are the major and minor axis of the synthesised beam defined as full width at half maximum, respectively.

In order to convert the CO map to an H₂ column density map we use (Schuster et al. 2007):

$$N_{\text{H}_2} = 0.25 \frac{X_{\text{MW}}}{0.8} \frac{T_{\text{CO}}}{\text{K km s}^{-1}}, \quad (5)$$

where $X_{\text{MW}} = 2.3 \times 10^{20} \text{ cm}^{-2} (\text{K km s}^{-1})^{-1}$ is the CO-to-H₂ conversion factor as determined for the Milky Way (Schuster et al. 2007) and T_{CO} is the velocity integrated CO intensity given as main beam antenna temperature. The factor 0.8 reflects the assumed 2-1/1-0 CO intensity ratio.

Both atomic and molecular gas maps were first converted to their corresponding mass surface densities. To convert from the observed integrated intensities to the total gas surface densities,

we use the relation $\Sigma_{\text{gas}} = 1.36(\Sigma_{\text{H1}} + \Sigma_{\text{H2}})$ taking into account the mass contribution from He. The distribution of Σ_{gas} is presented in Fig. 5. As in [Hitschfeld et al. \(2009\)](#), we use total mass surface density threshold in order to define spiral arm regions. These regions were chosen to be similar to those in interferometric CO maps, in H α maps, and in 1400 MHz radio continuum maps. All pixels with $\Sigma_{\text{gas}} > 25 \text{ M}_{\odot} \text{ pc}^{-2}$ were attributed to the spiral arm regions and pixels with $8 \text{ M}_{\odot} \text{ pc}^{-2} \leq \Sigma_{\text{gas}} \leq 25 \text{ M}_{\odot} \text{ pc}^{-2}$ were attributed to the inter-arm regions. We defined two additional regions in the cores of M 51 and NGC 5195 with a radius of $25''$. The resulting map and the defined regions are shown in Fig. 5.

3.4. Non-thermal radio spectral index and curvature

In the next step, we explore the observed non-thermal radio continuum spectra in different regions of the galaxy on a point-by-point basis. We fit a model spectrum consisting of a power law and a curvature component using a polynomial equation in logarithmic space ([Perley & Butler 2013, 2017a](#)):

$$\log S_{\nu} = \log S_0 + \alpha_0 \log(\nu/\nu_0) + \beta [\log(\nu/\nu_0)]^2, \quad (6)$$

where S_{ν} is the flux density at a given frequency, ν in GHz, S_0 is the flux density at the normalization frequency $\nu_0 = 1 \text{ GHz}$, α_0 is the non-thermal radio spectral index, β the non-thermal radio spectral curvature. Note that $\beta < 0$ corresponds to a concave spectrum. The non-thermal radio spectral index α_0 needs to be defined at a single reference frequency, because the spectral slope is frequency dependant in case of a curved spectrum. We start with this purely phenomenological model in order to explore the general shape of the spectrum without bias toward a specific physical mechanism. We explore the underlying physics responsible for the shape of the spectrum in Sect. 4.

For each point in the maps we fit this model to eight data points at frequencies listed in table 2 (excluding 619 MHz). For simplicity, we ignore higher-order terms and more sophisticated modeling of the spectra needs to be deferred to future work. The data are fitted with Levenberg–Marquardt least-squares algorithm. The resulting maps of best-fit α_0 and β , and their corresponding error maps are shown in Fig. 6. The reduced χ^2 of the fit is shown in Fig 7. The resulting parameter values are restricted to the frequency range between 54 and 8350 MHz and cannot be extrapolated towards arbitrary high or low frequencies.

The non-thermal radio spectral index at 1 GHz has values between -1.0 and -0.5 . The flatter radio spectra (α_0 from -0.7 to -0.5) are mostly found along the spiral arms where the star-forming regions are located. The inter-arm regions have radio spectral indices between -1.0 and -0.8 . The tidal bridge region between M 51 and NGC 5195 (located north of M 51) is characterized by a similarly steep radio spectrum, whereas the spectrum flattens again towards the companion with spectral indices of $\alpha_0 \approx -0.7$. Errors lie usually below 0.04 and only rise to 0.10 in regions of lower signal-to-noise ratios. Our radio spectral index map is very similar to the 1400–4850 MHz map by [Fletcher et al. \(2011\)](#), who used a 1400 MHz map from the VLA instead of the WSRT map (and the same 4850 MHz map we use). Our radio spectral index is defined at a lower frequency of 1 GHz, and so deviations of 0.1–0.2 become apparent in regions where the absolute value of the spectral curvature is high.

The spectral curvature is negative with values between -0.3 and 0.0. This means the radio spectrum is concave, implying a suppression of radio emission at either low or high frequencies, or a combination of both. The suppression of radio emission at low frequencies can happen be due to free–free absorption,

ionisation losses or synchrotron self absorption and at high frequency can happen due to CR radiation losses [Longair \(2011\)](#). We further explore which process is responsible for the observed curvature in Sect. 4. Regions with flatter radio spectra tend to show stronger curvatures ($\beta \leq -0.2$). Errors for the curvature are usually smaller than 0.06; only in regions with lower signal-to-noise ratios they can rise to 0.14. The reduced χ^2 is smaller than one in most of the galaxy, the value is higher in the areas where the error on the fit parameters is also high. The areas where the model doesn't fit the data so well also have a somewhat lower curvature. We assume that a better model in those areas would be just a power law.

3.5. Low- and high-frequency non-thermal radio spectral indices

We now study the non-thermal spectral index both at low and high frequencies. We compare the two-point low-frequency radio spectral index α_{low} between 54 and 144 MHz with the two-point high-frequency spectral index α_{high} between 1370 and 4850 MHz. The two-point spectral indices were calculated in a standard way by taking the logarithmic ratio of the flux densities in two maps over the logarithmic ratio of frequencies. The errors in the spectral index maps are calculated by propagating the errors from the individual maps which are a combination of the flux error (listed in Table 2) and the rms noise measured away from the source. The two-point spectral index maps are shown in Fig. 8. The reason for not selecting the two highest frequencies is the smaller extent of the galaxy at 8350 MHz, which would prevent us from studying the radio spectral index of the diffuse emission further in the outskirts of M 51. Additionally, skipping the 8350 MHz map gives a higher ratio between frequencies which results in a more reliable spectra index map.

On a cursory look, the maps of α_{low} and α_{high} have a similar morphology, but α_{low} is systematically higher than α_{high} . Values for α_{low} reach from -0.7 to 0.2 with errors in the range of 0.17 – 0.25 . In contrast, values for α_{high} reach from -1.3 to -0.6 with errors in the range of 0.05 – 0.15 . Higher errors for the low-frequency spectral index are expected because of the higher calibration error and noise in those maps. The errors are also higher at the edges of the maps because of a lower signal-to-noise ratio. The higher values of $\alpha_{\text{high}} \approx -0.7$ correlate well with the spiral arm structure of M 51, which has already been shown by [Fletcher et al. \(2011\)](#). The values of α_{low} are of similar apparent distribution, although the spiral arms are more diffuse and have an inverted radio spectrum as indicated by radio spectral indices with values of up to ~ 0.2 . Because of the cosmic ray radiation losses of the CR electrons, we expect a steepening at the edges of the galaxy. This is exactly what we see in the α_{low} map even if it might not be completely reliable because of the low signal-to-noise in these regions. We attribute the strong flattening of the radio spectrum at higher frequencies towards the extreme north and south as visible in the map of α_{high} as spurious. They are likely due to the limitations of combining the interferometric and single-dish data ([Cotton 2017](#)). These data do not affect our results as they are outside of our region of interest that we consider for our analysis (Sect. 2).

As the results of fitting for spectral index and curvature already suggested (Fig. 6), we see an overall flattening of the spectral index towards lower frequencies for the whole inner disc of M 51. In the following, we discuss the possible effects causing these flat and partially inverted spectra.

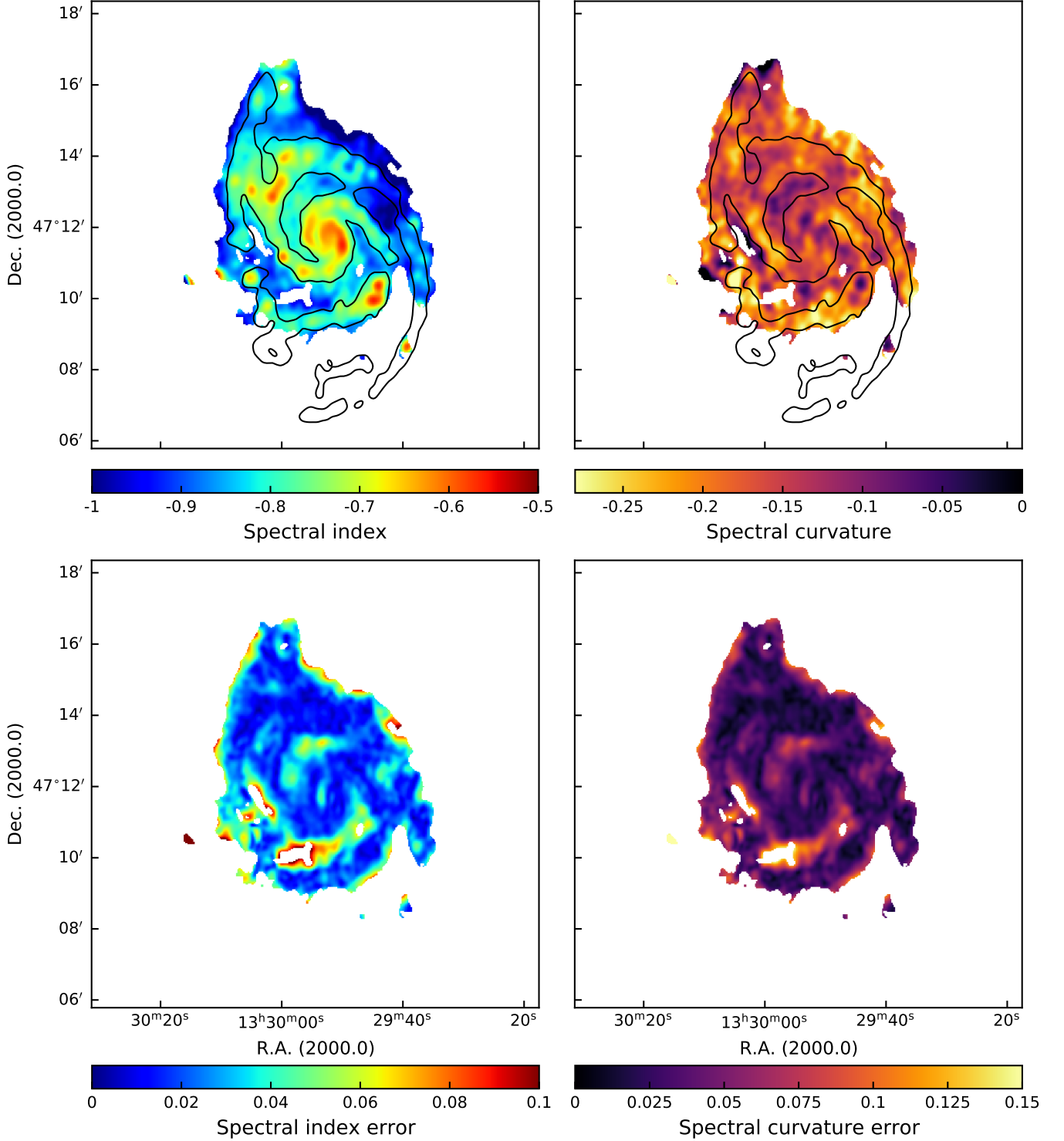


Fig. 6: Non-thermal radio spectral index and curvature at 1 GHz. Top panels: Best-fit radio spectral index α_0 (left panel) and spectral curvature (right panel). Bottom panels show the corresponding uncertainty maps of the radio spectral index (left panel) and curvature (right panel). The black contours represent a total gas mass surface density $25 M_{\odot} \text{pc}^{-2}$.

4. Spectral index flattening and low-frequency turnovers

Changes of spectral indices over frequency may be due to a number of reasons. In the following we investigate the plausible mechanisms that can alter the radio continuum spectrum from a power-law to a concave spectrum. This can be done

either by changing the cosmic-ray electron spectrum or by directly absorbing low-frequency radio emission. Previous work has shown (Heesen et al. 2023, 2024) that the diffusion coefficient of GeV CR electrons is energy-independent, at least over the relevant range in energies. Hence, we do not expect diffusion to change the spectrum. Also, advection does not change the spectrum. Hence, we now consider cosmic-ray radiation losses,

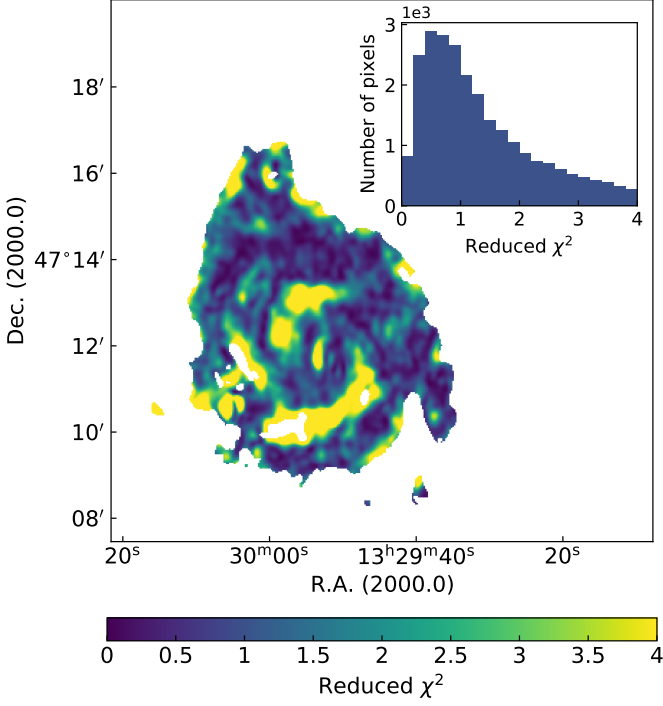


Fig. 7: Map of the reduced χ^2 of the fit presented in Fig. 6. The inset on the top right shows the histogram of the reduced χ^2 values.

synchrotron self-absorption, thermal free–free absorption, and cosmic-ray ionisation losses.

4.1. Cosmic-ray radiation losses

In regions of low gas densities, cosmic-ray electrons lose their energy due to synchrotron and inverse Compton radiation losses, causing their spectra to age, i.e. steepen.

In particular, spectral ageing predominantly affects the high-frequency radio spectral index (Sect. 3.5). We find that near star-forming regions the values of $\Delta\alpha = \alpha_{\text{low}} - \alpha_{\text{high}}$ are lower (between 0.2 and 0.5) compared to the inter-arm regions, where they are between 0.8 and 1.1. A proper modeling of CR ageing is not possible given the data but we can make a few qualitative observations. Fig. 6 clearly shows that the curvature is high, and the spectral index is lower in regions with low star-formation, i.e., in the inter-arm regions. Inside the spiral arms, the synchrotron emission at low frequencies is likely to be a mix of recently accelerated CR electrons and those from previous, nearby sites of star formation which fall within your resolution element. However, this is not true in the inter-arm regions where star formation is low. We have a resolution of approximately $16''$, i.e. 650 kpc. Assuming that the bulk of the CR electrons are produced in the arms, then CR electrons with energies lower than about 1.5 GeV will be able to diffuse to scales larger than 650 kpc (assuming $B = 10 \mu\text{G}$, and $D = 2 \cdot 10^{28} \text{ cm}^2/\text{s}$). This corresponds to CR electrons emitting at critical frequencies of 600–700 MHz. Hence, CR electrons emitting above 1 GHz, will lose energy before they get the chance to mix, especially in the inter-arm regions. Note, even in low star formation regions, the local CR electron injection timescale is much longer than the aging timescale. This is quantitatively shown in Fig. 3 of Basu et al. (2015) in order to explain steep spectra in low-density regions.

This argument is also supported by spatially resolved radio-FIR relation (see Fig. 5 and Section 4 of Basu et al. 2012).

4.2. Synchrotron self-absorption

Synchrotron self-absorption is known to play a key role in the flattening of spectra in the inner cores of Active Galactic Nuclei (AGN). We use the equation from Lacki (2013) to determine the turnover frequency ν_{SSA} for integrated spectra of galaxies

$$\nu_{\text{SSA}} = 2.4 \text{ MHz} \left(\frac{\Sigma_{\text{SFR}}}{50 \text{ M}_{\odot} \text{ yr}^{-1} \text{ kpc}^{-2}} \right)^{0.39}, \quad (7)$$

where Σ_{SFR} is the star-formation rate surface density. With a value of $\Sigma_{\text{SFR}} = 0.9$ from González-Lópezlira et al. (2013), we calculate a value of $\nu_{\text{SSA}} = 0.5 \text{ MHz}$. This value is by more than two orders of magnitude lower than our lowest observing frequency. Therefore, synchrotron self-absorption cannot be a dominant effect causing the flattening.

Similarly, diffuse large-scale structures in nearby galaxies are not very likely to be affected by synchrotron self-absorption due to the needed high magnetic field strength. We can calculate this magnetic field strength B_{SSA} for a given frequency ν in GHz and brightness temperature T_{b} in K using the standard equation:

$$B_{\text{SSA}} \approx 1.4 \cdot 10^{21} \nu T_{\text{b}}^{-2}. \quad (8)$$

T_{b} is defined as

$$T_{\text{b}} = 1.222 \cdot 10^3 \frac{I}{\nu^2 \theta_{\text{maj}} \theta_{\text{min}}} \text{ K}, \quad (9)$$

with the brightness I in Jy/beam and θ_{maj} and θ_{min} the synthesised major and minor beam half-power beam widths in arcseconds, respectively. Inserting our beam size of $17.5'' \times 15''$ and a brightness of 150 mJy/beam at 54 MHz as a maximum we end up with a magnetic field of $1.3 \times 10^{15} \text{ G}$. From equipartition calculations we know that the typical magnetic field strength in nearby galaxies is $9 \mu\text{G}$ (Beck 2005) with maximum values for extreme starburst cases like M 82 of $100 \mu\text{G}$ (Adebahr et al. 2013). Lacki (2013) discussed the possible turnover frequency for extreme starburst cases, which would be around $\nu_{\text{SSA}} = 2.4 \text{ MHz}$. These results show that synchrotron self-absorption cannot play an important role in the flattening of the spectra at low frequencies in M 51.

4.3. Thermal free–free absorption

Free–free absorption is an effect caused by an ionised medium, which absorbs radio waves while they propagate through it. The amount of absorption depends on the thermal electron number density n_e , the path length, and the frequency, such that the optical depth increases with decreasing frequency. Free–free absorption has been observed at frequencies below 500–1000 MHz in the core regions (Adebahr et al. 2013; Varenus et al. 2016) and individual star-forming regions (Wills et al. 1997; Varenus et al. 2015; Basu et al. 2017) of starburst galaxies, and also in the Milky Way (Rishbeth 1958; Roy & Rao 2004). Observations at very low radio frequencies also showed a turnover for the global spectrum of the Milky Way at about 3 MHz (Brown 1973).

In the following we investigate if free–free absorption can explain the flattening of the radio spectrum towards lower frequencies. Following Wills et al. (1997), the spectrum in case of free–free absorption of sources inside an ionised medium is

$$S_{\nu} = S_0 \nu_0^{\eta} e^{-\tau_{\text{ff}}}, \quad (10)$$

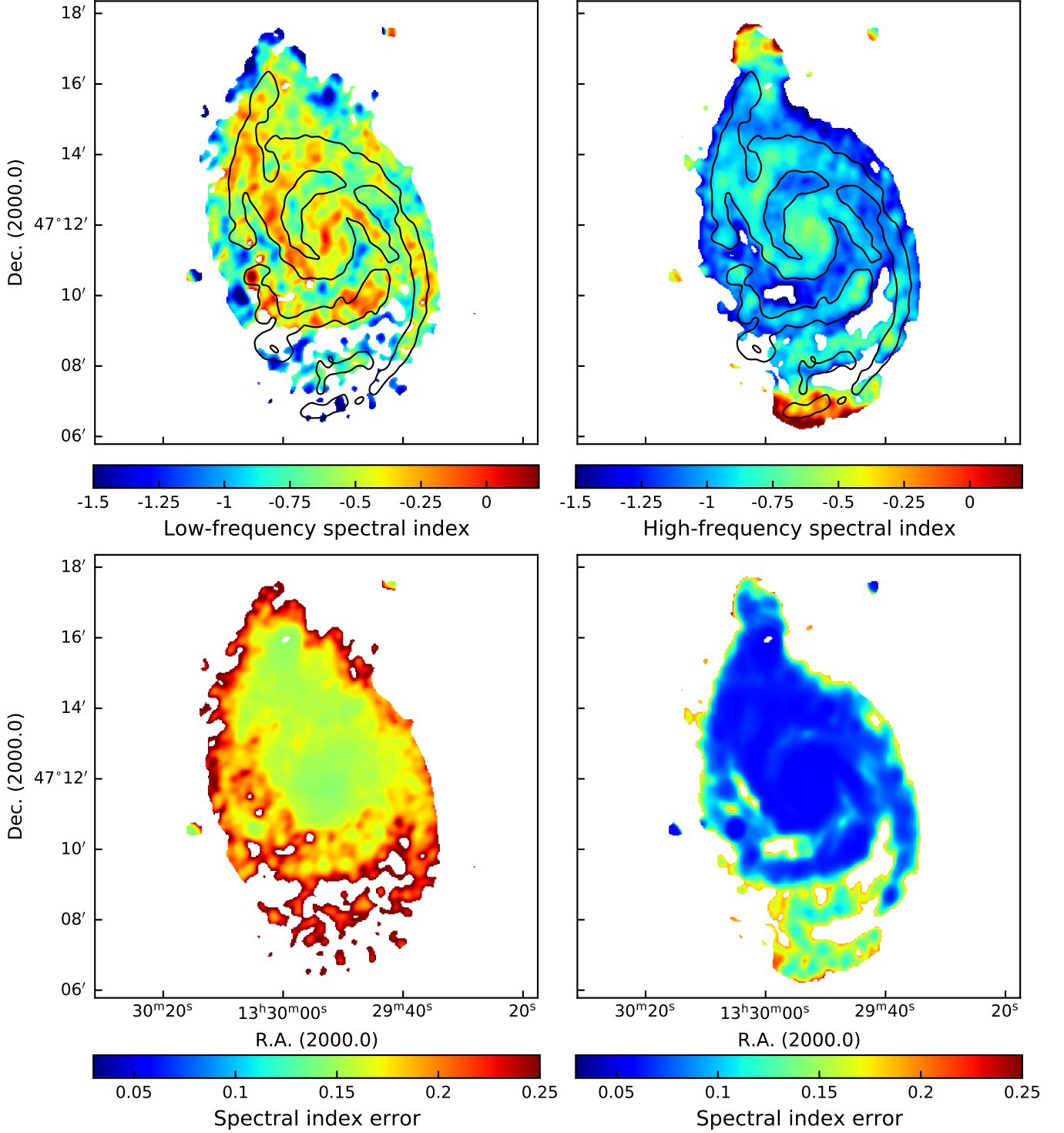


Fig. 8: Two point non-thermal radio spectral indices at low (α_{low} ; 54–144 MHz) and high (α_{high} ; 1370–4850 MHz) frequencies. The top panels show the spectral indices α_{low} (left panel) and at α_{high} (right panel). Bottom panels show the corresponding uncertainty maps. The black contours represent a total gas mass surface density $25 M_{\odot} \text{pc}^{-2}$.

with η the radio spectral index of the optically thin medium, and τ_{ff} the free-free emission optical depth. Taking the expression for the free-free Gaunt factor at radio wavelengths from [Lequeux \(2005\)](#), the optical depth is given as

$$\tau_{\text{ff}} = 8.2 \times 10^{-2} \nu_0^{-2.1} T_e^{-1.35} \text{EM}, \quad (11)$$

with the emission measure (EM) in units of $\text{cm}^{-6} \text{pc}$ and the electron temperature T_e in K. The EM is defined as

$$\left(\frac{\text{EM}}{\text{pc cm}^{-6}} \right) = \int_0^{s_0} \left(\frac{n_e}{\text{cm}^{-3}} \right)^2 \left(\frac{ds}{\text{pc}} \right), \quad (12)$$

where n_e is the thermal free electron density, and s is the distance along line-of-sight between the source at s_0 and observer

Table 3: Fitted parameters for the spectra of the spiral arm (SA), inter-arm (IA) and core (N5194c, N5195c) regions. Columns (2)–(4) are for free–free absorption and Columns (5)–(7) are for the curved spectral model, both are fitted to the non-thermal radio continuum spectra.

Region	S_0 [Jy]	η	EM [pc cm $^{-6}$]	S_0 [Jy]	α_0	β
SA $_{\text{syn}}$	0.630 ± 0.036	-0.839 ± 0.039	2800 ± 990	0.697 ± 0.013	-0.777 ± 0.0089	-0.176 ± 0.013
IA $_{\text{syn}}$	0.459 ± 0.026	-0.914 ± 0.041	2000 ± 790	0.507 ± 0.026	-0.881 ± 0.024	-0.147 ± 0.034
N5194c $_{\text{syn}}$	0.293 ± 0.014	-0.746 ± 0.032	2710 ± 980	0.3119 ± 0.0071	-0.674 ± 0.012	-0.144 ± 0.016
N5195c $_{\text{syn}}$	0.0917 ± 0.0036	-0.865 ± 0.027	2040 ± 570	0.09924 ± 0.0021	-0.821 ± 0.0097	-0.132 ± 0.014

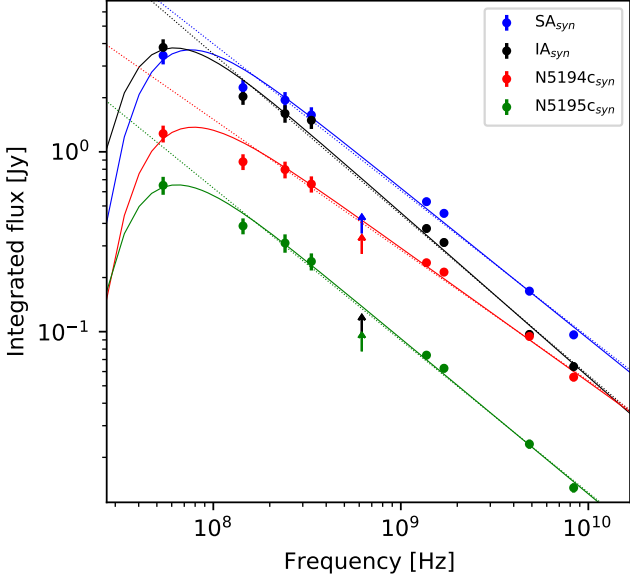


Fig. 9: Non-thermal radio continuum spectra for the spiral arm (SA), inter-arm (IA), and core regions (N5194c and N5195c). The flux densities at 619 MHz are only given as lower limits and are not included in the analysis. Solid lines are the best-fitting free–free absorption models (Eq. 10). Dotted lines show the power-law fits for frequencies ≥ 144 MHz.

at 0. The absorption model (Eq. 10) was used to fit the spectrum of M 51. We then derived the EM using Eq. (11), where we inserted the electron temperature as expressed by the galactocentric distance (Eq. 3).

4.3.1. Local radio continuum spectra

We first investigate the effect of free–free absorption on our radio continuum spectra analysing the integrated flux densities within the four regions of the arm, inter-arm, and two cores of, both, M 51 and NGC 5195 (Sect. 3.3). The thermal emission which we have previously subtracted is also affected by free–free absorption. However, we can ignore the absorption of the thermal radio continuum as free–free absorption is only significant at low frequencies where the thermal fraction is very low. Similarly, at high frequencies free–free absorption is negligible. We can therefore justify using the non-thermal maps as produced above for the fitting and neglect the effect of free–free absorption on the thermal emission. For comparison, we also fit the polynomial model (Eq. 6) to the non-thermal radio continuum spectra

(after thermal subtraction) in the four regions. The flux density error was estimated by assuming a statistical error caused by the map noise σ_{rms} as well as a relative flux uncertainty ϵ_v due to calibration uncertainty (see Table 2). The error of the flux-density measurements at each frequency is calculated using the following expression (Heesen et al. 2022):

$$\sigma_{S_\nu} = \sqrt{\left(\sigma_{\text{rms}} \sqrt{N_{\text{beams}}}\right)^2 + \left(\epsilon_v S_\nu\right)^2}, \quad (13)$$

where S_ν is the flux density and N_{beams} is the number of beams in the integration region.

Figure 9 shows the measured spectra within the regions together with the best-fitting absorption models. We show additional point spectra in Appendix B. The flattening of the spectra at low frequencies is highlighted by comparing the spectrum to a power law. The resulting parameters are listed in Table 3. The radio spectral indices η lie between -0.91 and -0.75 . For the polynomial fits, we find non-thermal radio spectral indices at 1 GHz between -0.88 and -0.67 .

We find that the EM has values between 2000 and 2800 cm $^{-6}$ pc. They mostly show the same tendency as the absolute values of the spectral curvature, as the higher values of EM are seen in the spiral arm regions, and the lower values in the inter-arm regions. However, the values of EM do not show a statistically significant difference because of high uncertainties.

4.3.2. Emission Measure and radio spectral index

We now investigate the free–free absorption on a point-by-point basis in order to determine the spatial distribution of the EM. For each point in the radio maps we fit the free–free absorption model (Eq. 10) to eight data points at frequencies listed in table 2 (excluding 619 MHz). We assume the electron temperature from Eq. 3. The parameters of the model which we fit are the spectral index η and the EM. We present the resulting maps in Fig. 10. In general, regions with higher gas densities (the spiral arms) show flatter spectral indices and slightly higher EM. While the steeper spectral index in the inter-arm regions can be explained by radiation losses of the cosmic-ray electrons during propagation away from their places of origin in the star-forming regions, the significant flattening in the spiral arms and in the cores of NGC 5194 and 5195 is difficult to explain without thermal absorption effects. The spectra presented in Fig. 9 show that the 54 MHz data points have much lower flux densities than what would be expected if the emission were to follow a power law. This is an indication of a flattening at low frequencies which is, at least in part, caused by free–free absorption.

We used the H α flux density map obtained using integral field unit spectroscopy to calculate and independent estimate of

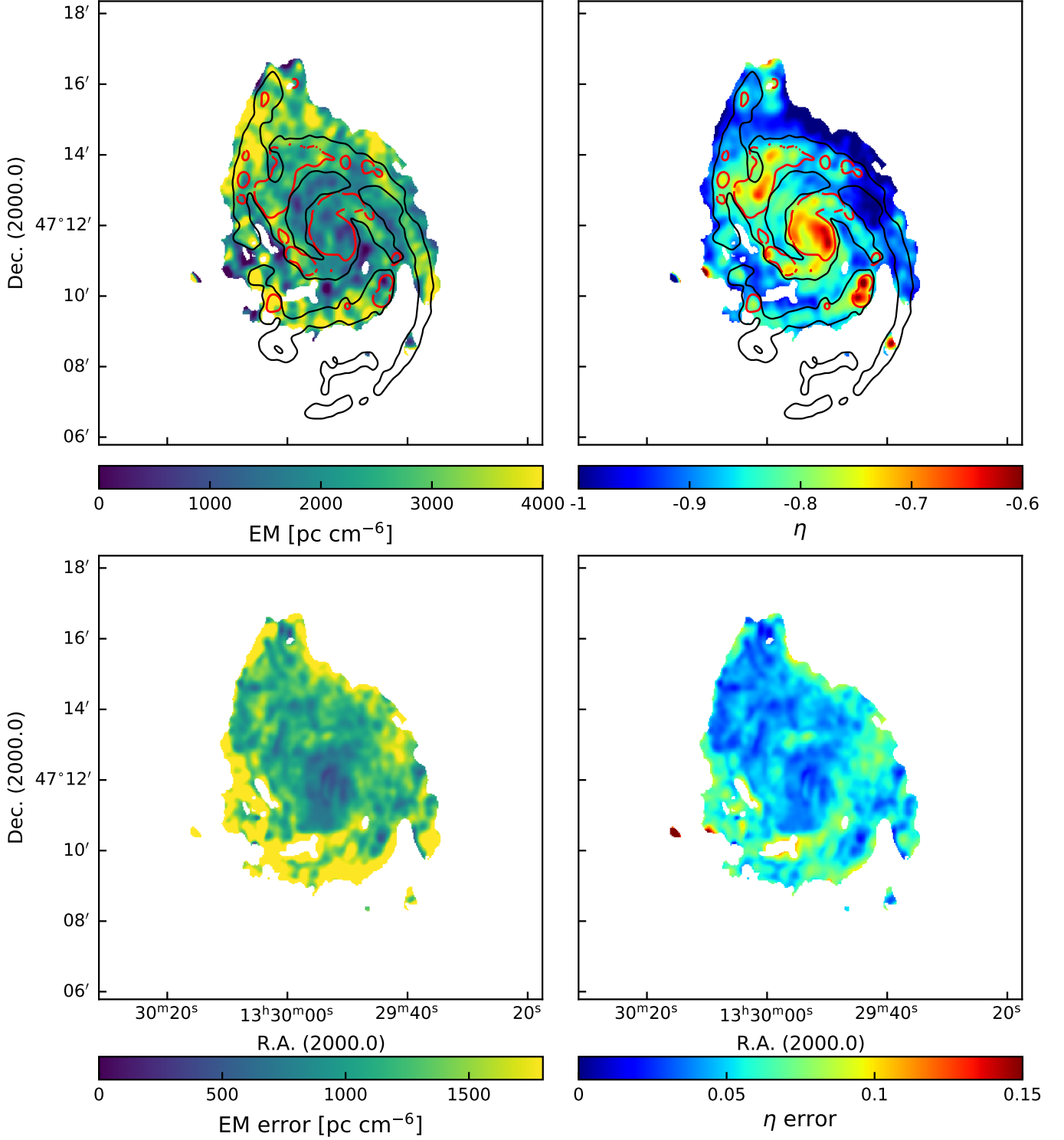


Fig. 10: Thermal free–free absorption: Shown are the results from fitting the thermal absorption model to the non-thermal radio continuum emission at eight frequencies between 45 and 8350 MHz (Table 2). The left column shows the resulting EM map (top panel) and its uncertainty map (bottom panel). The right column shows the radio spectral index of the optically thin medium η (top panel) and its uncertainty map (bottom panel). The red contours represent the H α flux value of $2.6 \cdot 10^{-13} \text{ erg s}^{-1} \text{ cm}^{-2} \text{ \AA}^{-1} \text{ beam}^{-1}$ from the Metal-THINGS survey. The black contours represent a total gas mass surface density $25 M_{\odot} \text{ pc}^{-2}$.

EM. We first convolved the data to the same beam as the radio maps. To calculate the EM, we used the equation (Dettmar 1992):

$$\text{EM} = 5 \cdot 10^{17} F_{H\alpha} / \Omega \text{ cm}^{-6} \text{ pc}, \quad (14)$$

where $F_{H\alpha}$ is the measured flux in $\text{erg cm}^{-2} \text{ s}^{-1}$ and $\Omega = 1.133 \cdot 17''.5 \times 15''.0$ is the collecting area in \square'' calculated for our beam.

We compare the EM from H α flux density to the EM obtained by fitting the free–free absorption model to the radio data by plotting them against each other in Fig. 11. Contrary to our

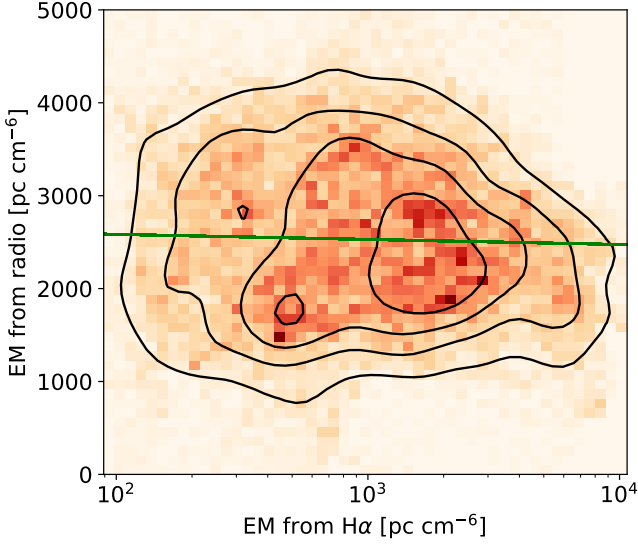


Fig. 11: Comparison of the EM from H α flux density to the EM obtained by fitting the free–free absorption model to the radio data. Colours and contours represent the data point density. The green line shows the best-fitting, albeit insignificant, correlation.

expectation, we see no correlation with a Spearman rank correlation coefficient of $\rho_s = -0.04$. This leads us to believe free–free absorption might not be the main mechanism responsible for the low-frequency flattening that we observe (see Sect. 4.4). An alternative reason could be that H α directly traces the clumpy ionised gas, while EM estimated from the radio spectrum also has contribution from the diffuse gas. The latter is known as the diffuse ionised gas that fills the space between the H II regions (Haffner et al. 2009). The radio free–free emission also originates from such a medium. The lack of correlation, or putative anti-correlation, may be hence explained by the very different volume filling factors.

4.4. Ionisation losses

We do, however, find a correlation between the spectral curvature and the H I gas mass surface density (Fig. 12). This leads us to explore ionisation losses as an alternative mechanism to explain the low frequency flattening because it dominates in the neutral gas. Cosmic-ray electrons lose energy due to the ionisation of atomic and molecular hydrogen. The ionisation loss rate is directly proportional to the number density of neutral atoms and molecules n , as can be seen from the following expression in the case of neutral hydrogen (Longair 2011):

$$-\left(\frac{dE}{dt}\right)_{\text{ion}} = 7.64 \times 10^{-15} n (3 \ln \gamma + 19.8) \text{ eV s}^{-1}, \quad (15)$$

where E is the electron energy, and γ is the Lorentz factor. The dependence on energy is only logarithmic so it can be approximated as constant throughout the spectrum. At lower energies a larger fraction of energy is lost due to ionisation and therefore the effect is stronger. Note that the fraction of energy lost is higher at lower CR energies because the total energy is lower while the lost energy is approximately constant. This means that the cosmic-ray electron number density (per energy bin) does decrease as function of time and this effect is more pronounced at lower energies. The spectral index flattening due to ionisation

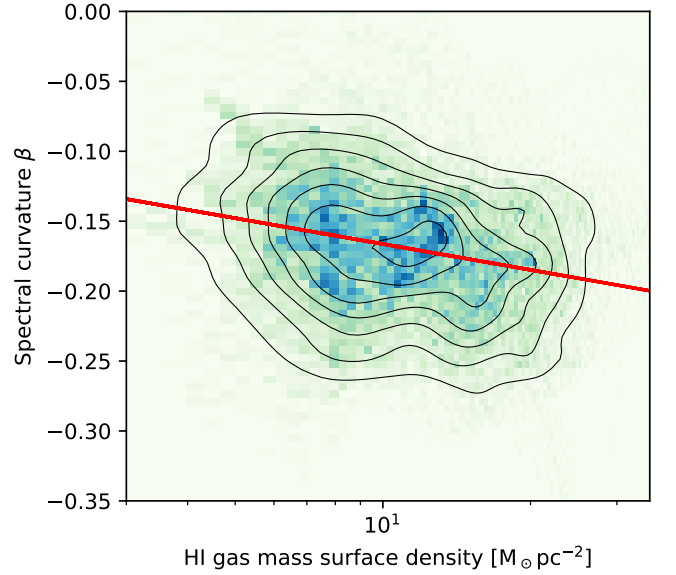


Fig. 12: Non-thermal radio spectral curvature as function of the H I gas mass surface density. Colours and contours show the data point density. The red line shows the best-fitting correlation.

losses should be $\Delta\alpha \leq 0.5$ in comparison to the injection spectrum (Basu et al. 2015).

In Fig. 12 we show the non-thermal spectral curvature as function of H I gas mass surface density. We find a weak negative correlation ($\rho_s = -0.21$). This can be explained if cosmic-ray ionisation losses are causing the low frequency flattening. At higher H I gas mass surface densities, the spectrum becomes more concave (lower value of β), as one would expect if ionisation losses play a role. The time-scale for ionisation losses is (Murphy 2009):

$$t_{\text{ion}} = 4.1 \times 10^9 \left(\frac{n}{\text{cm}^{-3}}\right)^{-1} \left(\frac{E}{\text{GeV}}\right) \left[3 \ln\left(\frac{E}{\text{GeV}}\right) + 42.5\right]^{-1} \text{ yr}. \quad (16)$$

Hence, in order to be an important process to flatten the radio continuum spectrum at low frequencies, this time-scale has to be shorter than the synchrotron loss time-scale of approximately 100 Myr (Heesen et al. 2023). For our cosmic-ray electrons with $E \approx 0.5$ GeV at the lowest frequency, we thus expect $t_{\text{ion}} \approx 100$ Myr for neutral gas densities of $n \approx 0.5 \text{ cm}^{-3}$. This is the case for mass surface densities of $\Sigma_{\text{gas}} = 2.5\text{--}5 \text{ M}_{\odot} \text{ pc}^{-2}$, assuming a gas scale height of 100 pc (Cox 2005; Basu et al. 2015). This means the suggested correlation between non-thermal spectral curvature and H I gas mass surface density can indeed be ascribed to cosmic-ray ionization losses that affect the low-energy cosmic-ray electrons the most. In the absence of a spectral model for ionisation losses, we leave more rigorous fitting of the spectra to future work. For now, we cannot rule out the effect free–free absorption in addition to ionisation losses. Hence, we conclude that the low-frequency flattening observed in M 51 is probably caused by a combination of ionisation losses and free–free absorption.

Ionisation of the molecular component of the interstellar medium should also cause CR energy loss. We repeated the same analysis shown in Fig. 12 to test the correlation between the spectral curvature and the total gas mass density. Contrary to our expectation, they were not found to be correlated ($\rho_s = -0.07$). A possible reason is that the cosmic rays (at least in the GeV-

range) do not enter molecular clouds, due to the strong and turbulent magnetic field (Tabatabaei et al. 2013).

5. Summary and conclusions

Synchrotron spectra at low radio frequencies are shaped by several processes such as cosmic-ray ionisation losses and free-free absorption that suppress the emission. The cosmic-ray energy loss from ionisation is nearly independent of energy (only logarithmic dependence) so it proportionally affects low-energy cosmic-ray electrons the most, resulting in spectral flattening. Free-free absorption is also strongly dependent on frequency with frequencies below 300 MHz (depending on EM) being more affected. This affects our ability to interpret low-frequency continuum emission as an extinction-free star formation tracer. On the other hand, strong free-free absorption would allow us to measure the EM which itself is, derived from radio spectra, an extinction-free star-formation tracer. In order to study these effects we compiled data of the nearby grand-design spiral galaxy M 51 at nine different frequency bands between 54 and 8350 MHz of which we used eight for the analysis. We present here, for the first time, new observation with the GMRT at 240 MHz. We calculated the contribution of the thermal radio continuum emission based on the H α map corrected for extinction using 24 μ m mid-infrared data. This contribution was subtracted from the radio maps so we studied only the non-thermal emission. We also used new integral field unit spectroscopy data from Metal-THINGS in order to measure extinction-corrected H α intensities which we use as an independent estimate of EM.

First, we fit a polynomial function to the logarithmic intensities to determine the non-thermal radio spectral index and spectral curvature as shown in Fig. 6. The non-thermal radio spectral index at 1 GHz is relatively flat in the spiral arms with $\alpha_0 \approx -0.6$, in agreement with the injection spectral index. The spectral curvature is negative throughout the galaxy with more negative values in the spiral arms. This means the spectrum is concave where intensities both at low and high frequencies are suppressed. This is the expected behaviour for low-energy losses and absorption effects as well as strong synchrotron and inverse Compton radiation losses at higher frequencies resulting in spectral ageing. Next, we calculated the low- (54–144 MHz) and high-frequency (1370–4850 MHz) non-thermal two-point radio spectral indices separately as shown in Fig. 8. The low-frequency radio spectral index is very flat and even positive in the spiral arms with α_{low} between -0.5 and 0.2 , showing the presence of inverted radio continuum spectra. This clearly hints at either low frequency absorption or cosmic-ray ionisation losses. In contrast, the high-frequency radio spectra are fairly steep with values of α_{high} between -1.5 and -0.7 . The differences throughout the galaxy can be explained by spectral ageing.

Next we analysed the spatially resolved spectral index in more detail, starting with the effect of free-free absorption. In Fig. 9 we plotted the integrated spectra of the spiral arms, inter-arm and core regions. We find that the spectra can be well fitted with a free-free absorption model (Wills et al. 1997). At 54 MHz the deviation from a power-law spectrum is most apparent.

Comparing the spiral arms with the inter-arm regions, we find that in the spiral arms the turnover occurs at higher frequencies, which implies stronger free-free absorption. This is confirmed by the values of the EM obtained by fitting the free-free absorption model. On the other hand, the difference in EM between spiral arm and inter-arm regions is not statistically significant, suggesting that free-free absorption might not be the only effect.

We then fitted the free-free absorption model to our spatially resolved data. We obtain point-by-point maps of the EM and the radio spectral index η (Fig. 10). We compare the values of EM obtained from the fit to the values estimated from the extinction-corrected H α measurements. We do not see a correlation between the EM's calculated from different tracers (Fig. 11). The lack of correlation, may be hence explained by the very different volume filling factors or it is possible that the free-free absorption is not the only process which causes the low frequency flattening. Therefore, we also investigated the possible influence of cosmic-ray ionisation losses on the radio continuum spectrum. To this end, we study the correlation between non-thermal spectral curvature and gas mass surface density. We find a weak correlation between spectral curvature and H I gas mass surface density (Fig. 12). This leads us to believe that the main process responsible for the low-frequency flattening is more dominant in the regions with neutral H I gas. In those regions the cosmic rays lose energy due to ionisation. Because ionisation losses are nearly frequency-independent, they are more apparent at low frequencies where we observe emission from low energy cosmic-ray electrons. We therefore conclude that the low frequency flattening in M 51 is most likely caused by a combination of free-free absorption and ionisation losses.

This is the first time that we observe a low-frequency spectral flattening in an average spiral galaxy outside of the Milky Way. Previously, this effect has only been observed in starburst galaxies (Adebahr et al. 2013; Basu et al. 2015; Varenus et al. 2016; Adebahr et al. 2017). Now we were able to spatially locate the region of the galaxy where the spectra flattens at low frequencies and find that those areas generally have a higher density of H I gas. Curiously, we do not find significant correlation between spectral curvature and total gas mass density, suggesting that the cosmic-ray ionisation losses are in the atomic gas phase but not in the molecular gas phase. Possibly because the cosmic rays do not enter molecular clouds due to the magnetic field (Tabatabaei et al. 2013). We also want to consider what our results mean for using sub-GHz radio continuum observations as a SFR tracer. Even using low frequencies of around 150 MHz (LOFAR HBA) as a SFR tracer requires an understanding of the losses we investigate here (see e.g. Adebahr et al. 2013; Chyzy et al. 2018). The forthcoming surveys with LOFAR at very low frequencies and high angular resolution will enable further studies in other nearby galaxies and allow us to investigate the influence of these effects in more detail.

Acknowledgements. We thank the two anonymous referees for detailed comments which significantly improved the paper and especially made it more understandable for the reader. LG and MB acknowledge funding by the Deutsche Forschungsgemeinschaft (DFG, German Research Foundation) under Germany's Excellence Strategy – EXC 2121 “Quantum Universe” – 390833306. BA, DJB and MS acknowledge funding from the German Science Foundation DFG, via the Collaborative Research Center SFB1491 ‘Cosmic Interacting Matters – From Source to Signal’. FdG acknowledges support from the ERC Consolidator Grant ULU 101086378. LOFAR (van Haarlem et al. 2013) is the Low Frequency Array designed and constructed by ASTRON. It has observing, data processing, and data storage facilities in several countries, which are owned by various parties (each with their own funding sources), and that are collectively operated by the ILT foundation under a joint scientific policy. The ILT resources have benefited from the following recent major funding sources: CNRS-INSU, Observatoire de Paris and Université d’Orléans, France; BMBF, MIWF-NRW, MPG, Germany; Science Foundation Ireland (SFI), Department of Business, Enterprise and Innovation (DBEI), Ireland; NWO, The Netherlands; The Science and Technology Facilities Council, UK; Ministry of Science and Higher Education, Poland; The Istituto Nazionale di Astrofisica (INAF), Italy. This research made use of the Dutch national e-infrastructure with support of the SURF Cooperative (e-infra 180169) and the LOFAR e-infra group. The Jülich LOFAR Long Term Archive and the German LOFAR network are both coordinated and operated by the Jülich Supercomputing Centre (JSC), and computing resources on the supercomputer JUWELS at JSC were provided by the Gauss

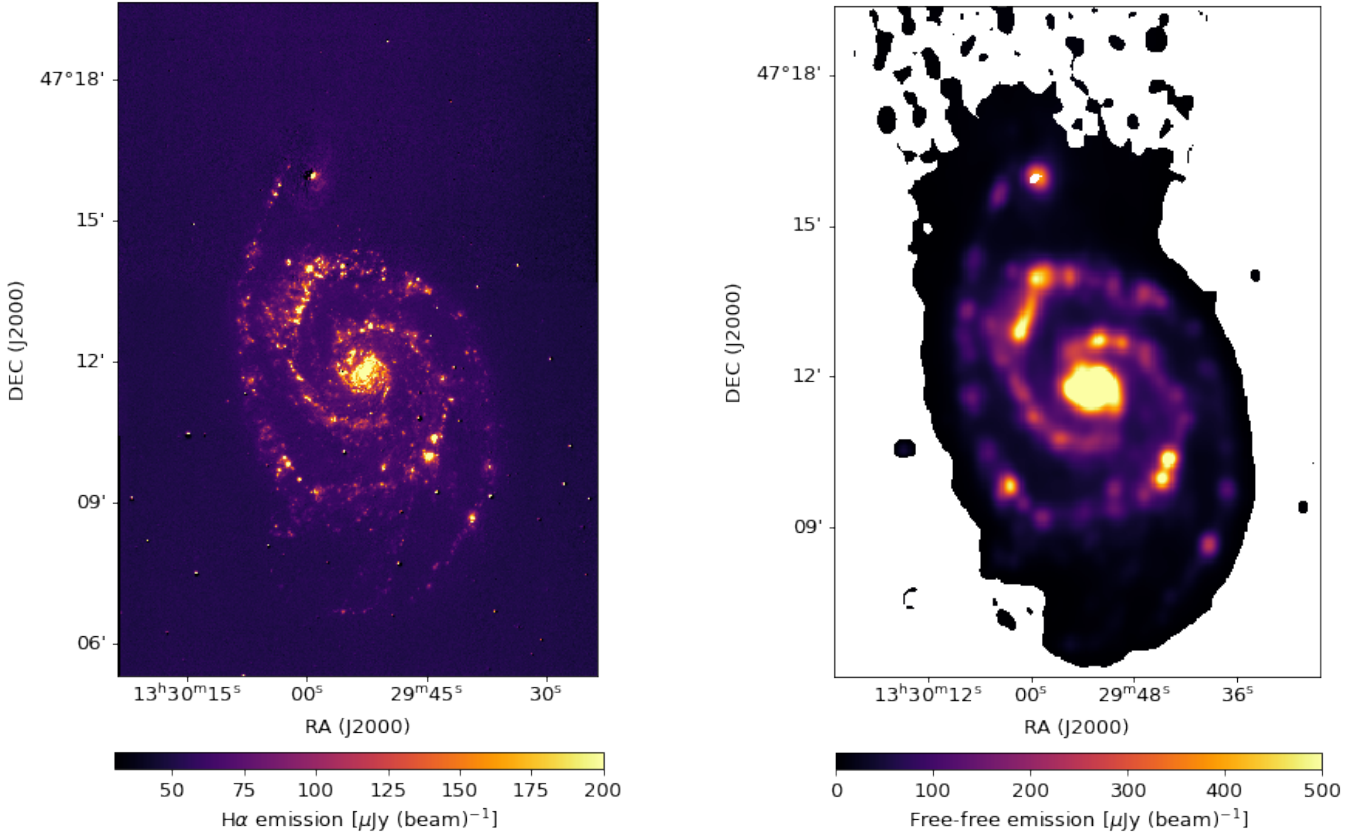
Centre for Supercomputing e.V. (grant CHTB00) through the John von Neumann Institute for Computing (NIC). This research made use of the University of Hertfordshire high-performance computing facility and the LOFAR-UK computing facility located at the University of Hertfordshire and supported by STFC [ST/P000096/1], and of the Italian LOFAR IT computing infrastructure supported and operated by INAF, and by the Physics Department of Turin university (under an agreement with Consorzio Interuniversitario per la Fisica Spaziale) at the C3S Supercomputing Centre, Italy. The research leading to these results has received funding from the European Research Council under the European Union's Seventh Framework Programme (FP/2007-2013) / ERC Advanced Grant RADIOLIFE-320745. The Westerbork Synthesis Radio Telescope is operated by ASTRON (Netherlands Foundation for Research in Astronomy) with support from the Netherlands Foundation for Scientific Research (NWO). This research made use of the Python Kapteyn Package (Terlouw & Vogelaar 2015).

References

- Adebahr, B., Krause, M., Klein, U., Heald, G., & Dettmar, R. J. 2017, *A&A*, 608, A29
- Adebahr, B., Krause, M., Klein, U., et al. 2013, *A&A*, 555, A23
- Alloin, D., Collin-Souffrin, S., Joly, M., & Vigroux, L. 1979, *A&A*, 78, 200
- Anantharamaiah, K. R., Viallefond, F., Mohan, N. R., Goss, W. M., & Zhao, J. H. 2000, *ApJ*, 537, 613
- Baars, J. W. M., Genzel, R., Pauliny-Toth, I. I. K., & Witzel, A. 1977, *A&A*, 61, 99
- Basu, A., Beck, R., Schmidt, P., & Roy, S. 2015, *MNRAS*, 449, 3879
- Basu, A., Mitra, D., Wadadekar, Y., & Ishwara-Chandra, C. H. 2012, *MNRAS*, 419, 1136
- Basu, A., Mitra, D., Wadadekar, Y., & Ishwara-Chandra, C. H. 2012, *MNRAS*, 419, 1136
- Basu, A., Roy, S., & Mitra, D. 2012, *ApJ*, 756, 141
- Basu, A., Roychowdhury, S., Heesen, V., et al. 2017, *MNRAS*, 471, 337
- Beck, R. 2005, in *The Magnetized Plasma in Galaxy Evolution*, ed. K. T. Chyzy, K. Otmianowska-Mazur, M. Soida, & R.-J. Dettmar, 193–200
- Beck, R. & Wielebinski, R. 2013, *Magnetic Fields in Galaxies*, ed. T. D. Oswalt & G. Gilmore, Vol. 5, 641
- Blandford, R. & Eichler, D. 1987, *Phys. Rep.*, 154, 1
- Braun, R., Oosterloo, T. A., Morganti, R., Klein, U., & Beck, R. 2007, *A&A*, 461, 455
- Bresolin, F., Garnett, D. R., & Kennicutt, Jr., R. C. 2004, *ApJ*, 615, 228
- Brown, L. W. 1973, *ApJ*, 180, 359
- Chyzy, K. T., Jurusik, W., Piotrowska, J., et al. 2018, *A&A*, 619, A36
- Cid Fernandes, R., Mateus, A., Sodré, L., Stasinska, G., & Gomes, J. M. 2011, *STARLIGHT: Spectral Synthesis Code, Astrophysics Source Code Library*, record ascl:1108.006
- Colombo, D., Meidt, S. E., Schinnerer, E., et al. 2014, *ApJ*, 784, 4
- Condon, J. J. 1992, *ARA&A*, 30, 575
- Condon, J. J., Cotton, W. D., Greisen, E. W., et al. 1998, *AJ*, 115, 1693
- Cornwell, T. J. & Perley, R. A. 1992, *A&A*, 261, 353
- Cotton, W. D. 2017, *PASP*, 129, 094501
- Cox, D. P. 2005, *ARA&A*, 43, 337
- de Gasperin, F., Williams, W. L., Best, P., et al. 2021, *A&A*, 648, A104
- Deeg, H.-J., Duric, N., & Brinks, E. 1997, *A&A*, 323, 323
- Dettmar, R. J. 1992, *Fund. Cosmic Phys.*, 15, 143
- Farnes, J. S., Green, D. A., & Kantharia, N. G. 2013, *ArXiv e-prints*
- Fletcher, A., Beck, R., Shukurov, A., Berkhuijsen, E. M., & Horellou, C. 2011, *MNRAS*, 412, 2396
- Gioia, I. M., Gregorini, L., & Klein, U. 1982, *A&A*, 116, 164
- González-Lópezlira, R. A., Pflamm-Altenburg, J., & Kroupa, P. 2013, *ApJ*, 770, 85
- Gould, R. J. 1975, *ApJ*, 196, 689
- Green, D. A. 2014, *Bulletin of the Astronomical Society of India*, 42, 47
- Haffner, L. M., Dettmar, R. J., Beckman, J. E., et al. 2009, *Reviews of Modern Physics*, 81, 969
- Hales, S. E. G., Waldram, E. M., Rees, N., & Warner, P. J. 1995, *MNRAS*, 274, 447
- Han, J. L. 2017, *ARA&A*, 55, 111
- Heald, G. H., Pizzo, R. F., Orrú, E., et al. 2015, *A&A*, 582, A123
- Heesen, V., de Gasperin, F., Schulz, S., et al. 2023, *A&A*, 672, A21
- Heesen, V., Schulz, S., Brüggem, M., et al. 2024, *A&A*, 682, A83
- Heesen, V., Staffehl, M., Basu, A., et al. 2022, *A&A*, 664, A83
- Hitschfeld, M., Kramer, C., Schuster, K. F., Garcia-Burillo, S., & Stutzki, J. 2009, *A&A*, 495, 795
- Hu, T., Shao, Z., & Peng, Q. 2013, *ApJ*, 762, L27
- Hummel, E. 1991, *A&A*, 251, 442
- Ignesti, A., Vulcani, B., Poggianti, B. M., et al. 2022, *ApJ*, 924, 64
- Intema, H. T. 2014, in *Astronomical Society of India Conference Series*, Vol. 13, Astronomical Society of India Conference Series, 469
- Intema, H. T., Jagannathan, P., Mooley, K. P., & Frail, D. A. 2017, *A&A*, 598, A78
- Intema, H. T., van der Tol, S., Cotton, W. D., et al. 2009, *A&A*, 501, 1185
- Israel, F. P. & Mahoney, M. J. 1990, *ApJ*, 352, 30
- Karachentsev, I., Lebedev, V., & Shcherbanovskii, A. 1985, *Bulletin d'Information du Centre de Données Stellaires*, 29, 87
- Kennicutt, R., Armus, L., Bendo, G., et al. 2003, *PASP*, 115, 928
- Kennicutt, R. C., Hao, C.-N., Calzetti, D., et al. 2009, *ApJ*, 703, 1672
- Klein, U., Wielebinski, R., & Morsi, H. W. 1988, *A&A*, 190, 41
- Konar, C., Hardcastle, M. J., Jamroz, M., & Croston, J. H. 2013, *MNRAS*, 430, 2137
- Lacki, B. C. 2013, *MNRAS*, 431, 3003
- Lal, D. V., Lyskova, N., Zhang, C., et al. 2022, *ApJ*, 934, 170
- Lane, W. M., Cotton, W. D., Helmboldt, J. F., & Kassim, N. E. 2012, *Radio Science*, 47, RS0K04
- Lara-López, M. A., Pilyugin, L. S., Zaragoza-Cardiel, J., et al. 2023, *A&A*, 669, A25
- Lara-López, M. A., Zinchenko, I. A., Pilyugin, L. S., et al. 2021, *ApJ*, 906, 42
- Lequeux, J. 2005, *The Interstellar Medium*
- Li, J.-T., Beck, R., Dettmar, R.-J., et al. 2016, *MNRAS*, 456, 1723
- Lisenfeld, U. & Völk, H. J. 2000, *A&A*, 354, 423
- Longair, M. S. 2011, *High Energy Astrophysics*, Cambridge University Press, 3rd Edition, chapter 19
- Marvil, J., Owen, F., & Eilek, J. 2015, *AJ*, 149, 32
- McQuinn, K. B. W., Skillman, E. D., Dolphin, A. E., Berg, D., & Kennicutt, R. 2016, *ApJ*, 826, 21
- Meyer, M., Robotham, A., Obreschkow, D., et al. 2017, *PASA*, 34, 52
- Mulcahy, D. D., Fletcher, A., Beck, R., Mitra, D., & Scaife, A. M. M. 2016, *A&A*, 592, A123
- Mulcahy, D. D., Horneffer, A., Beck, R., et al. 2014, *A&A*, 568, A74
- Mulcahy, D. D., Horneffer, A., Beck, R., et al. 2018, *A&A*, 615, A98
- Murphy, E. J. 2009, *ApJ*, 706, 482
- Niklas, S., Klein, U., & Wielebinski, R. 1997, *A&A*, 322, 19
- Offringa, A. R., McKinley, B., Hurley-Walker, N., et al. 2014, *MNRAS*, 444, 606
- Pagel, B. E. J., Edmunds, M. G., Blackwell, D. E., Chun, M. S., & Smith, G. 1979, *MNRAS*, 189, 95
- Perley, R. A. & Butler, B. J. 2013, *ApJS*, 204, 19
- Perley, R. A. & Butler, B. J. 2017a, *ApJS*, 230, 7
- Perley, R. A. & Butler, B. J. 2017b, *ApJS*, 230, 7
- Pohl, M. & Schlickeiser, R. 1990, *A&A*, 239, 424
- Pohl, M., Schlickeiser, R., & Hummel, E. 1991a, *A&A*, 250, 302
- Pohl, M., Schlickeiser, R., & Lesch, H. 1991b, *A&A*, 252, 493
- Rishbeth, H. 1958, *MNRAS*, 118, 591
- Roberts, I. D., van Weeren, R. J., Lal, D. V., et al. 2023, *arXiv e-prints*, arXiv:2310.20417
- Roy, S. & Pramesh Rao, A. 2006, in *Journal of Physics Conference Series*, Vol. 54, 156–160
- Roy, S. & Rao, A. P. 2004, *MNRAS*, 349, L25
- Sault, R. J., Teuben, P. J., & Wright, M. C. H. 1995, in *Astronomical Society of the Pacific Conference Series*, Vol. 77, *Astronomical Data Analysis Software and Systems IV*, ed. R. A. Shaw, H. E. Payne, & J. J. E. Hayes, 433
- Schlafly, E. F. & Finkbeiner, D. P. 2011, *ApJ*, 737, 103
- Schuster, K. F., Kramer, C., Hitschfeld, M., Garcia-Burillo, S., & Mookerjee, B. 2007, *A&A*, 461, 143
- Shimwell, T. W., Hardcastle, M. J., Tasse, C., et al. 2022, *A&A*, 659, A1
- Stasińska, G., Collin-Souffrin, S., Joly, M., & Alloin, D. 1981, *A&A*, 93, 362
- Steer, D. G., Dewdney, P. E., & Ito, M. R. 1984, *A&A*, 137, 159
- Stein, M., Heesen, V., Dettmar, R. J., et al. 2023, *A&A*, 670, A158
- Swarup, G., Ananthakrishnan, S., Kapahi, V. K., et al. 1991, *Current Science*, 60, 95
- Tabatabaei, F. S., Schinnerer, E., Krause, M., et al. 2017, *ApJ*, 836, 185
- Tabatabaei, F. S., Schinnerer, E., Murphy, E. J., et al. 2013, *A&A*, 552, A19
- Tasse, C. 2014, *A&A*, 566, A127
- Tasse, C., Hugo, B., Mirmont, M., et al. 2018, *A&A*, 611, A87
- Terlouw, J. P. & Vogelaar, M. G. R. 2015, *Kapteyn Package*, version 2.3, Kapteyn Astronomical Institute, Groningen, available from <http://www.astro.rug.nl/software/kapteyn/>
- Tremblin, P., Anderson, L. D., Didelon, P., et al. 2014, *A&A*, 568, A4
- van Haarlem, M. P., Wise, M. W., Gunst, A. W., et al. 2013, *A&A*, 556, A2
- Varenius, E., Conway, J. E., Martí-Vidal, I., et al. 2016, *A&A*, 593, A86
- Varenius, E., Conway, J. E., Martí-Vidal, I., et al. 2015, *A&A*, 574, A114
- Walter, F., Brinks, E., de Blok, W. J. G., et al. 2008, *AJ*, 136, 2563
- Wills, K. A., Pedlar, A., Muxlow, T. W. B., & Wilkinson, P. N. 1997, *MNRAS*, 291, 517

Appendix A: Thermal subtraction

Fig. A.1: Intermediate data products in the subtraction of thermal emission in M 51.



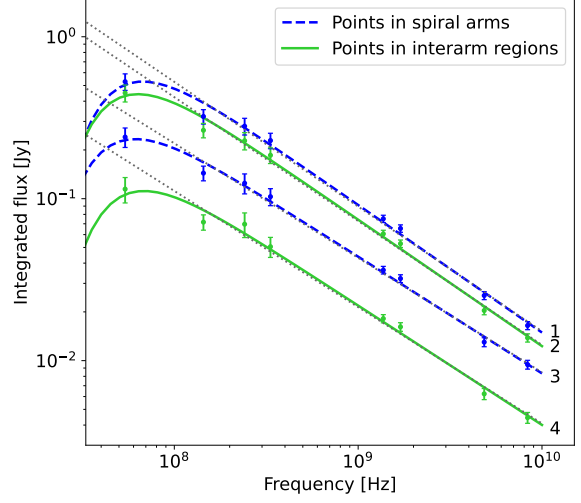
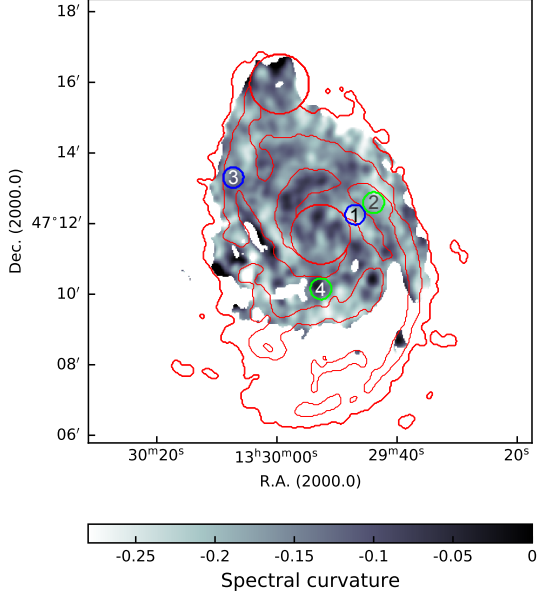
(a) Initial continuum-subtracted $H\alpha$ map obtained with the Kitt Peak National Observatory 2.1-m telescope using the narrow-band $H\alpha$ -filter KP1563 (Kennicutt et al. 2003). The angular resolution is $1''.35 \times 1''.35$ and the rms noise is $\approx 50 \mu\text{Jy beam}^{-1}$. The map was downloaded from the ancillary data at the SINGS webpage.^a

(b) Extinction corrected prediction of the free-free emission at 1370 MHz in M 51. This emission was scaled to the appropriate frequency with the spectral index $\alpha = 0.1$. The map shown here was subtracted from the radio maps to get the non-thermal emission. The beam size is $17''.5 \times 15''.0$.

^a <http://irsa.ipac.caltech.edu/data/SPITZER/SINGS/>

Appendix B: Point spectra

Fig. B.1: Individual point spectra.



(a) The location of individual spectra from spiral arms (interarm regions) marked by green (blue) circles on top of the spectral curvature map. The size of the circles corresponds to the beam size. Red contours at 8 and 25 $M_{\odot} \text{pc}^{-2}$ define the borders of the spiral arm and inter-arm regions, respectively (Sect. 3.3).

(b) Non-thermal radio continuum spectra for representative beam-sized regions marked in Fig. B.1a. Each spectrum is labeled with its corresponding number. Dotted lines show the power-law fits for frequencies ≥ 144 MHz. The individual spectra show the same trends as the integrated spectra in Fig. 9.